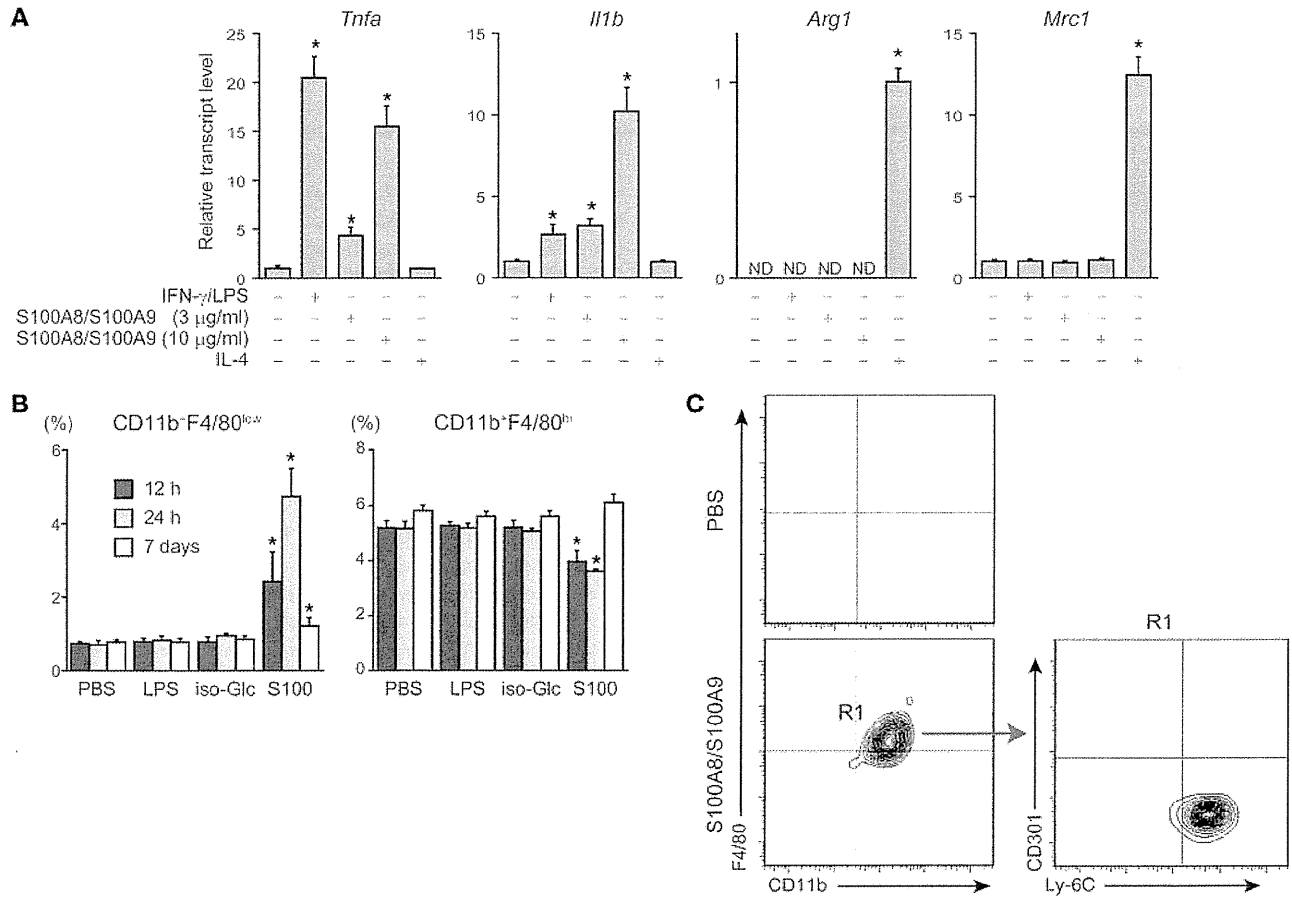

Figure 8

S100A8 and S100A9 induce M1-type activation and accumulation of CD11b$^+$F4/80^{lo} cells. (**A**) Effects of S100A8/A9 on M1 or M2 activation of BMDMs. Unstimulated BMDMs were treated with IFN-γ plus LPS, S100A8 plus S100A9 (3 and 10 μg/ml of each), or IL-4 for 24 hours, and expression of M1 and M2 markers was analyzed. Expression levels were normalized to those of 18s rRNA and then further normalized to the levels in BMDMs without stimulation, except *Arg1*. *$P < 0.05$ versus untreated control. $n = 3$. (**B**) Effect of renal injection of recombinant S100A8 and S100A9 on macrophage accumulation. A solution of recombinant S100A8 and S100A9 (S100; 25 μg of each protein) was injected directly into the right kidney. The same amount of vehicle PBS, PBS containing LPS at a concentration (9.2 pg/ml) matched to that in the S100A8/A9 solution (LPS), or PBS whose osmolarity was matched to that of the S100 solution using glucose (iso-Glc) was injected into kidneys as control. CD11b$^+$F4/80^{lo} and CD11b$^+$F4/80^{hi} fractions among total live cells were determined by flow cytometry. $n = 3$. *$P < 0.05$ versus kidneys 12 hours after PBS injection. (**C**) CD11b$^+$Ly-6C$^+$EGFP$^+$ BM cells (1×10^6 cells/mouse) were prepared from CAG-*EGFP* mice and adoptively transferred into wild-type mice prior to a single injection of PBS or S100A8 plus S100A9 (25 μg of each) into kidneys. Transferred EGFP$^+$ cells recruited to kidneys were analyzed by flow cytometry. Cells in R1 (CD11b$^+$F4/80^{lo}) were further analyzed for expression of Ly-6C and CD301.

cells within 12 hours (Figure 8B) and also induced moderate levels of apoptosis and tubular injury (Supplemental Figure 11). The controls, which included PBS, PBS containing LPS at a level matching that in the recombinant S100A8/A9 solution, or PBS whose osmolarity was matched to that of the S100A8/A9 solution using glucose, did not induce CD11b$^+$F4/80^{lo} cell accumulation (Figure 8B). The CD11b$^+$F4/80^{hi} M2-type macrophage fraction was reduced by S100A8/A9 injection, suggesting that S100A8 and S100A9 selectively recruit CD11b$^+$F4/80^{lo} cells to the kidneys and/or promote M1-type activation in recruited monocytes.

Previous studies have shown that CD11b$^+$Ly-6C$^+$ inflammatory monocytes are the major monocyte population recruited to kidneys 5 days after UUO (11). Therefore, prior to UUO we adoptively transferred BM CD11b$^+$Ly-6C$^+$ monocytes prepared from CAG-*EGPF* mice, in which *EGFP* was ubiquitously expressed (Supplemental Figure 12). One day after UUO, the transferred EGFP$^+$ monocytes were recruited to the kidneys, and the majority of them exhibited the CD11b$^+$F4/80^{lo}Ly-6C$^+$CD301$^-$ phenotype, while a minor population exhibited the CD11b$^+$F4/80^{hi}Ly-6C$^{-/lo}$CD301$^+$ M2-type phenotypes (Supplemental Figure 12A). In contrast, very few CD11b$^+$Ly-6C$^-$ BM monocytes were recruited to UUO kidneys (data not shown). Thus, as with monocytes transferred 5 days after UUO (11), CD11b$^+$Ly-6C$^+$ inflammatory monocytes appear to be the major source of monocytes recruited to kidneys early after UUO. The finding that expression of *Emr1* (F4/80) and *Il1b* was increased while expression of *Csf1r* (CD115), which is highly expressed in monocytes (26), was decreased indicates that the recruited CD11b$^+$F4/80^{lo} cells were differentiating into M1-type macrophages. This supports the notion that kidney CD11b$^+$F4/80^{lo} cells include macrophages and newly recruited monocytes differentiating into macrophages.

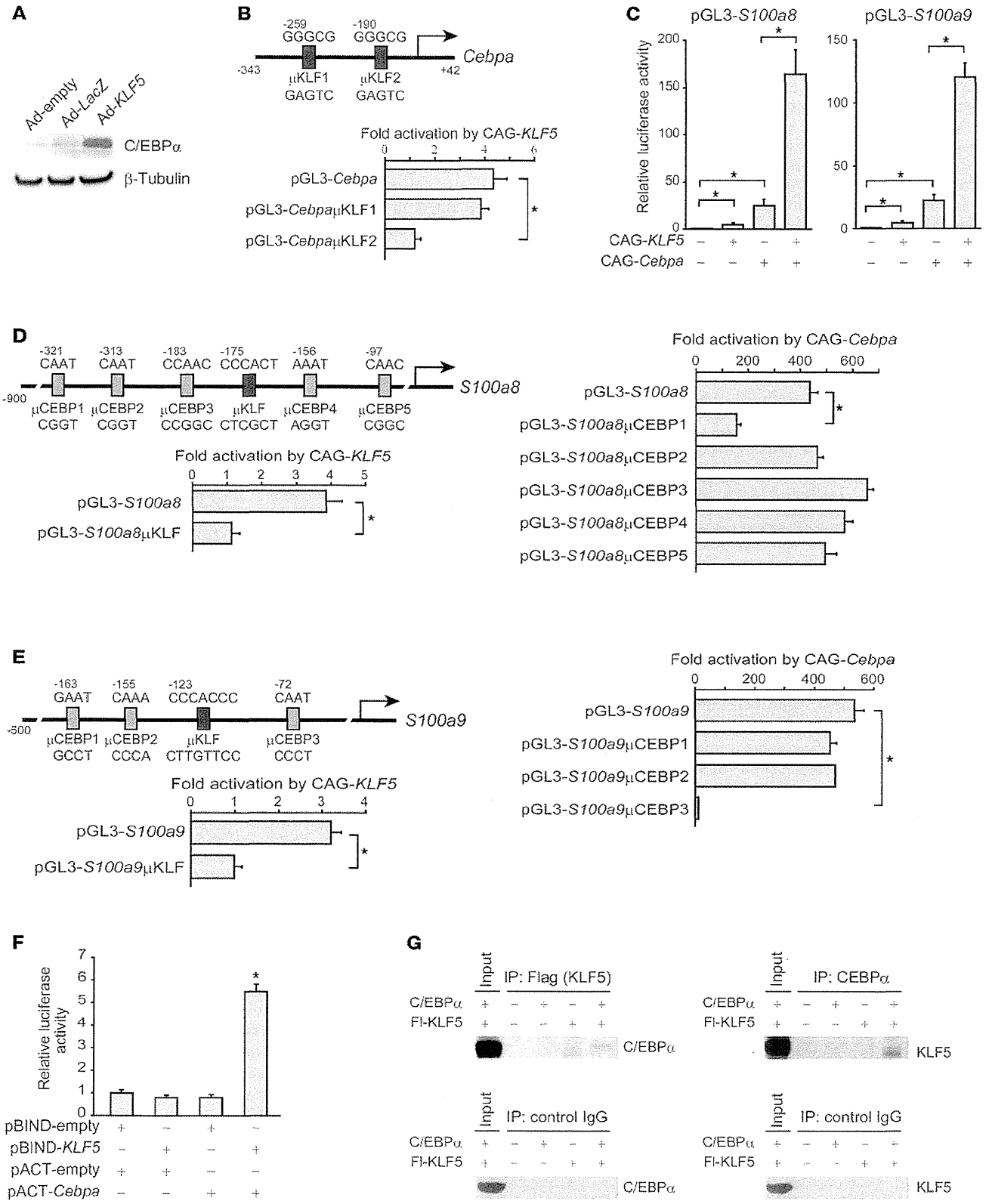

Figure 9
KLF5 transactivates the *Cebpa*, *S100a8*, and *S100a9* promoters. (**A**) Expression of C/EBPα protein in mIMCD-3 cells infected with Ad-empty, Ad-*LacZ*, or Ad-*KLF5*. (**B**) Effects of KLF5 on the activity of the *Cebpa* proximal promoter. mIMCD3 cells were transfected with *Cebpa* promoter reporter constructs containing the indicated mutations within the putative KLF5-binding sites plus either an empty (CAG-empty) or KLF5-encoding (CAG-*KLF5*) plasmid. The luciferase activity of each reporter construct cotransfected with CAG-*KLF5* was normalized to that of the reporter cotransfected with CAG-empty. Mutant sequences (indicated by μ) are shown schematically. $n = 6$. $^*P < 0.05$. (**C**) Effects of KLF5 and C/EBPα on *S100a8* and *S100a9* promoter activity. Luciferase reporters driven by the promoters were cotransfected with expression vectors for KLF5 and C/EBPα (CAG-*Cepba*), as indicated. Luciferase activity was normalized to that of the reporter construct cotransfected with CAG-empty. $n = 6$. (**D** and **E**) Relative activation of mutant *S100a8* and *S100a9* promoters by KLF5 and C/EBPα. Mutant sequences are shown schematically. $n = 6$. $^*P < 0.05$. (**F**) Mammalian two-hybrid analysis of the interaction between KLF5 and C/EBPα. mIMCD-3 cells were transfected with the indicated combinations of plasmids containing the Gal4-DNA binding domain fused to the full-length KLF5 (pBIND-*KLF5*) and the VP16-activation domain fused to the full-length C/EBPα (pACT-*Cebpa*), along with a reporter plasmid (pG5-luc). $n = 6$. $^*P < 0.05$ versus cells transfected with pBIND-empty and pACT-empty. (**G**) Physical interaction between KLF5 and C/EBPα. Lysates of mIMCD-3 cells expressing Flag-tagged KLF5 (Fl-KLF5) and C/EBPα were immunoprecipitated with antibody against Flag, C/EBPα, or control IgG. Immunoprecipitates were probed for C/EBPα or KLF5.

We next tested whether S100A8 and S100A9 might be capable of recruiting $CD11b^+Ly\text{-}6C^+$ monocytes. S100A8/A9 injection resulted in accumulation of $CD11b^+F4/80^{lo}Ly\text{-}6C^+CD301^-$ cells (Figure 8C). In contrast to UUO, S100A8/A9 injection did not induce M2-type differentiation. Following the injection, expression of *Emr1* and *Il1b* was increased, while *Csf1r* expression was decreased (Supplemental Figure 12C), indicating M1-type macrophage differentiation of recruited inflammatory monocytes in the kidneys.

We also tested whether injection of S100A8/A9 might rescue the wild-type phenotype in $Klf5^{+/-}$ kidneys. We found that S100A8/A9 increased the $CD11b^+F4/80^{lo}$ cell fractions in $Klf5^{+/-}$ kidneys to levels similar to those in wild-type kidneys, while decreasing the $CD11b^+F4/80^{hi}$ cell fraction (Supplemental Figure 13A). In addition, S100A8/A9 increased apoptosis and tubular injury, while suppressing interstitial fibrosis (Supplemental Figure 13B). Likewise, renal injury scores in $Klf5^{+/-}$ kidneys were similar to those in wild-type kidneys after S100A8/A9 injection, indicating that S100A8 and S100A9 are the key mediators regulated by KLF5 in response to UUO. Taken together, these results demonstrate that S100A8 and S100A9, which are induced by KLF5 in response to UUO, recruit $CD11b^+Ly\text{-}6C^+$ inflammatory monocytes to the kidneys and promote their M1-type differentiation in the monocytes.

KLF5 acts in concert with C/EBPα to control S100a8 and S100a9 expression. Previous in vitro studies suggest C/EBP transcription factors are involved in the control of *S100a8* and *S100a9* transcription (38–40), but it is not yet clear whether C/EBP proteins regulate the promoters in vivo. Interestingly, overexpression of *Klf5* led to increases in the expression of C/EBPα (Figure 9A and Supplemental Figure 14A), and ChIP-seq revealed that KLF5 binds to the *Cebpa* locus. Conversely, knocking down *Klf5* reduced levels of the *Cebpa* transcript and C/EBPα protein in mIMCD-3 cells (Supplemental Figure 14, B and C), suggesting KLF5 directly controls *Cebpa* expression. Consistent with this idea, a reporter plasmid containing a fragment spanning −343 to +42 bp of the *Cebpa* promoter was transactivated by KLF5 (Figure 9B). Furthermore, the *Cebpa* promoter contains two potential KLF5 binding motifs, at −259 and at −190 bp, and mutations within the motif at −190 bp abolished the KLF5-dependent transactivation.

We next conducted a series of reporter analyses to assess the functional involvement of KLF5 and C/EBPα in the transcriptional regulation of *S100a8* and *S100a9*. We found that the *S100a8* and *S100a9* promoters were transactivated by either KLF5 or C/EBPα and that their coexpression led to synergistic activation of the promoters (Figure 9C). Mutations within the potential KLF5 binding sites abolished KLF5-dependent activation of the promoters (Figure 9, D and E). Similarly, among the potential C/EBP binding sites, mutations within motifs at −321 bp of *S100a8* or −72 bp of *S100a9* significantly suppressed transactivation by C/EBPα. The synergistic transactivation of the *S100a8* and *S100a9* promoters by KLF5 and C/EBPα suggests the two transcription factors physically interact. Indeed, mammalian two-hybrid analysis showed that KLF5 and C/EBPα do interact during transcriptional regulation (Figure 9F), and coimmunoprecipitation assays showed that they physically associate with one another in mIMCD-3 cells (Figure 9G).

UUO switches KLF5 targets in vivo. To further characterize the transcriptional regulatory circuit, we used in vivo ChIP analyses to analyze the promoter binding of KLF5 and C/EBPα. Cells were isolated from renal papillae 24 hours after either UUO or control sham operation. In the control cells, KLF5 did not bind to *Cebpa*, *S100a8*, or *S100a9*, but it did bind to the *Cdh1* promoter (Figure 10A). This binding profile was reversed by UUO. Following UUO, KLF5 bound to the *Cebpa*, *S100a8*, and *S100a9* promoters, but binding to *Cdh1* was eliminated (Figure 10A). Correspondingly, whereas C/EBPα did not bind to the *S100a8* or *S100a9* promoter in control cells, it was recruited to those promoters by UUO (Figure 10B).

We then used sequential ChIP (re-ChIP) to determine whether KLF5 and C/EBPα simultaneously bind to the same promoters. Chromatin samples were prepared from renal papillary cells 12 and 24 hours after UUO. UUO induced KLF5 binding to *S100a8* and *S100a9* within 12 hours, but C/EBPα was not bound to the promoters at that time (Figure 10, C and D). The chromatin samples pulled down by KLF5 or C/EBPα antibody were then further immunoprecipitated with C/EBPα or KLF5 antibody, respectively. These re-ChIP assays showed that while C/EBPα did not bind to the KLF5-bound *S100a8* and *S100a9* promoters 12 hours after UUO (Figure 10, C and D), both KLF5 and C/EBPα were bound to the promoter 24 hours after UUO. This strongly suggests that UUO induces KLF5 binding to the *Cebpa*, *S100a8*, and *S100a9* promoters within 12 hours, and that the induction of *Cebpa* expression by KLF5 leads to cooperative transactivation of the *S100a8* and *S100a9* promoters by KLF5 and C/EBPα. As would be expected from this model, renal levels of *Klf5* transcript were increased within 4 hours after UUO, and this was followed by induction of *Cebpa* expression (Figure 11A). Levels of *S100a8*, *S100a9*, and *Ccl2* transcripts were increased within 12 hours, and levels of KLF5, C/EBPα, S100A8, and S100A9 proteins were clearly increased in whole kidneys 6–12 hours after UUO (Figure 11B). More specifically, KLF5, S100A8, and S100A9 proteins were increased in collecting duct cells 12 hours after UUO, but were undetectable in non-collecting duct cells (Figure 11C). As expected, levels of these mRNAs

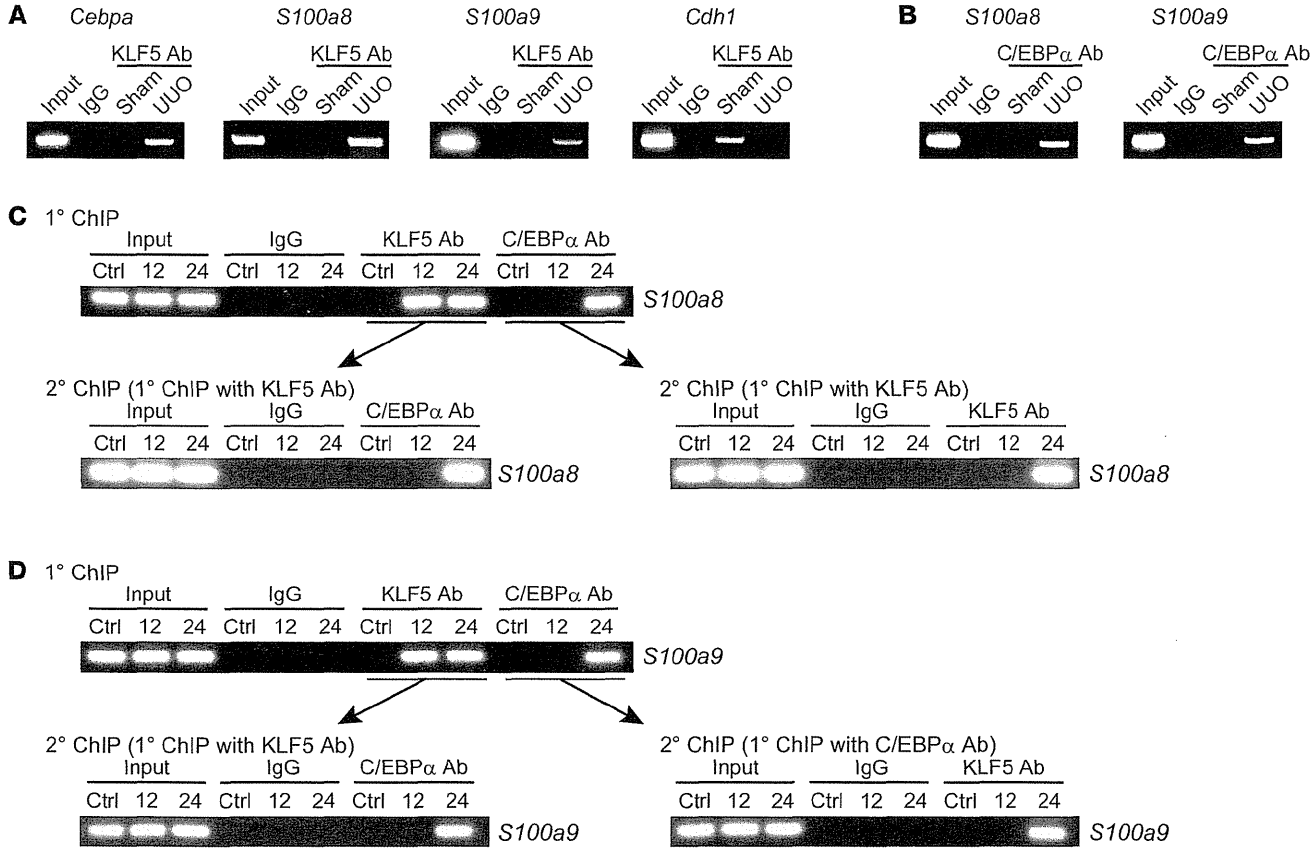

Figure 10
UUO alters KLF5 binding targets in vivo. (**A** and **B**) ChIP assays for KLF5 (**A**) and C/EBPα (**B**) binding to their target promoters in IMCD cells isolated from kidneys subjected to either UUO or sham operation. One percent of the input chromatin from IMCD cells isolated from the sham-operated kidneys was used as a positive control (Input). Samples prepared from UUO kidneys and immunoprecipitated with nonimmune IgG were used as a negative control. ChIP assays using a nontarget region (*Pdgfa* 3′UTR) as a negative control are shown in Supplemental Figure 15A. (**C** and **D**) In vivo re-ChIP analysis of the simultaneous binding of KLF5 and C/EBPα to the *S100a8* (**C**) and *S100a9* (**D**) promoters. Chromatin samples prepared from renal papillary cells of control (Ctrl) and 12- and 24-hour UUO kidneys were subjected to immunoprecipitation using KLF5 or C/EBPα antibody (1° ChIP). The immunoprecipitates were then pulled down further using C/EBPα or KLF5 antibody, respectively (2° ChIP). ChIP assays of a nontarget region (*Pdgfa* 3′UTR) are shown in Supplemental Figure 15B.

and proteins were all reduced in *Klf5*$^{+/-}$ kidneys (Figure 11, A, B, and D). By contrast, *CCl2* expression only differed on days 4 and 7 (Figure 11A).

The binding of KLF5 to the *Cdh1* promoter under basal conditions (Figure 10A) suggests KLF5 also regulates *Cdh1* expression. That notion is supported by the observations that *Cdh1* expression was reduced in *Klf5*$^{+/-}$ kidneys (Supplemental Figure 15C), that knocking down *Klf5* reduced *Cdh1* expression in mIMCD-3 cells (Supplemental Figure 15D), and that KLF5 transactivated the *CDH1* promoter (Supplemental Figure 15E). KLF5 thus appears to control *Cdh1* expression under basal conditions, and UUO switches the KLF5 target genes from *Cdh1* to *Cebpa*, *S100a8*, and *S100a9*.

KLF5 in renal collecting duct cells plays a central role in CD11b^{+}*F4/80*^{lo} *cell accumulation and renal damage.* In the kidney, *Klf5* is primarily expressed in renal collecting ductal cells (Figure 1, A–D, and Supplemental Figure 1C). However, occasional low-level KLF5 staining was observed in a few stromal cells, which could be fibroblasts and/or BMDCs. To further establish the importance of KLF5 expressed in collecting duct cells to renal injury, we carried out a set of BM transplantation experiments. When wild-type mice whose BM had been replaced with that from either wild-type or *Klf5*$^{+/-}$ mice subjected to UUO, the CD11b^{+}F4/80^{lo} fractions did not significantly differ between the two groups (Figure 12A), nor did levels of *Klf5*, *Cebpa*, *S100a8*, and *S100a9* expression (Figure 12B) and renal injury scores (Supplemental Figure 16).

To further rule out a possible contribution of KLF5 in macrophages to the observed renal *Klf5*$^{+/-}$ phenotypes, we selectively ablated *Klf5* in myeloid cells by crossing *Klf5* floxed mice (*Klf5*$^{fl/fl}$) with *LysM-Cre* mice (41). As a result, more than 95% of *Klf5* floxed alleles were deleted in kidney CD11b^{+}F4/80^{+} cells (Supplemental Figure 17A). This *Klf5* deficiency in macrophages did not affect the accumulation of CD11b^{+}F4/80^{lo} and CD11b^{+}F4/80^{hi} cells in UUO kidneys or their expression of cytokines (Figure 7, A and B, and Supplemental Figure 17B). Moreover, renal injury scores were unaffected by myeloid-specific *Klf5* deletion (Supplemental Figure 18).

To further confirm the importance of KLF5 expressed in

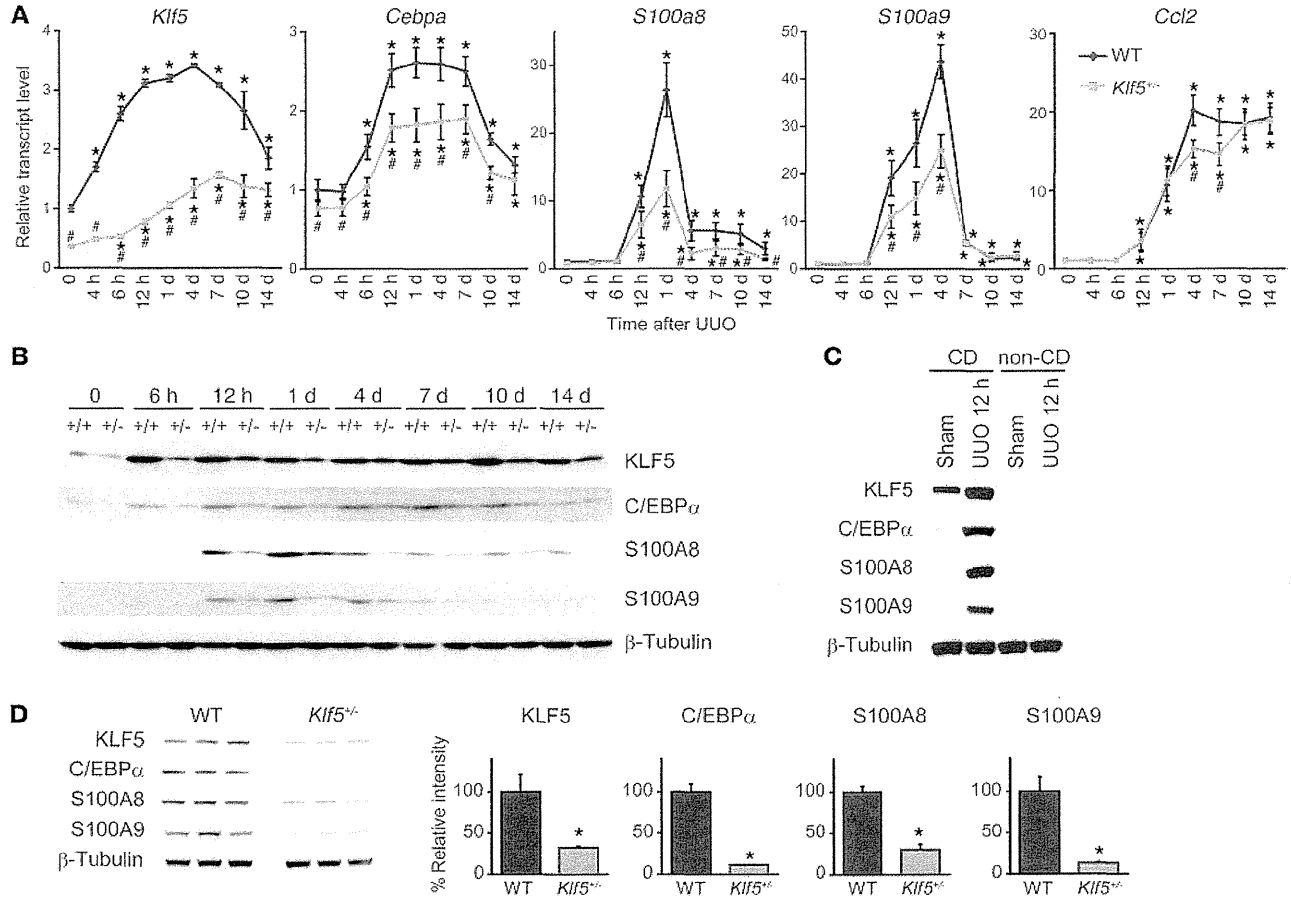

Figure 11

KLF5 is essential for induction of C/EBPα and S100A8/S100A9 in vivo. (**A**) Time course of *Klf5*, *Cebpa*, *S100a8*, *S100a9*, and *Ccl2* expression in kidneys from wild-type and *Klf5*$^{+/-}$ mice following UUO. Expression levels were normalized to those of 18s rRNA and then further normalized to the levels in the control wild-type kidney. Data labeled 0 show gene expression in kidneys under basal conditions. $n = 5$ for each group. $^{*}P < 0.05$ versus control kidneys of the same genotype; $^{\#}P < 0.05$ versus wild-type at the same time point. Note that some of the *Klf5* expression data are the same as in Figure 3A. (**B**) Time course of KLF5, C/EBPα, S100A8, and S100A9 protein expression after UUO in whole kidneys from wild-type (+/+) and *Klf5*$^{+/-}$ (+/–) mice. (**C**) Collecting duct–specific expression of KLF5, C/EBPα, S100A8, and S100A9 12 hours after UUO. KLF5, C/EBPα, S100A8, and S100A9 protein expression was analyzed in collecting duct (CD) and non–collecting duct (non-CD) cells prepared from sham-operated and 12-hour UUO kidneys. (**D**) Expression of KLF5, CEBPα, S100A8, and S100A9 proteins in CD cells isolated from wild-type and *Klf5*$^{+/-}$ kidneys 1 day after UUO. Relative intensities of the bands analyzed by quantitative densitometry are shown. $^{*}P < 0.05$ versus wild-type. $n = 3$.

the collecting duct, we selectively deleted *Klf5* from collecting duct cells by crossing *Klf5*$^{fl/fl}$ mice with *Aqp2-Cre* mice in which *Cre* expression was selectively driven in collecting duct cells by the *Aqp2* promoter (Supplemental Figure 19A). The efficacy of the *Klf5* deletion from collecting duct cells was approximately 70% (Supplemental Figure 19, B–D). Under basal conditions, *Klf5*$^{fl/fl}$*;Aqp2-Cre* mice did not show abnormal kidney histology or blood chemistry (i.e., creatinine and electrolyte levels) (Supplemental Figure 19E and Supplemental Table 4). In kidneys from the collecting duct–specific *Klf5*-knockout mice, accumulation of CD11b^{+}F4/80^{lo} cells (Figure 12C) and expression of *Klf5*, *Cebpa*, *S100a8*, and *S100a9* were significantly reduced, as compared with kidneys from *Klf5*$^{fl/fl}$ mice, 24 hours after UUO (Figure 12D). The apoptotic cell fractions and glomerular sclerosis and tubular injury scores were all reduced in *Klf5*$^{fl/fl}$*;Aqp2-Cre* mice, while interstitial fibrosis was enhanced, as compared with *Klf5*$^{fl/fl}$ mice (Supplemental Figure 18). Overall, the renal phenotypes of *Klf5*$^{fl/fl}$*;Aqp2-Cre* mice were largely comparable to those of *Klf5*$^{+/-}$ mice, indicating that KLF5 expressed in collecting duct cells is primarily responsible for the renal phenotypes observed in *Klf5*$^{+/-}$ mice and is essential for renal responses to UUO.

Discussion

The results of the present study demonstrate that renal collecting duct cells play a pivotal role in the response to renal injury (Figure 12E). In response to UUO, *S100a8* and *S100a9* expression is induced by KLF5. S100A8 and S100A9 in turn recruit CD11b^{+}Ly-6C^{+} inflammatory monocytes to the kidneys, and then contribute to the cells' differentiation into M1-type CD11b^{+}F4/80^{lo} cells, which promote renal epithelial injury and inflammation. Thereafter, the numbers of CD11b^{+}F4/80^{hi} M2-type cells, which promote fibrosis, gradually increase. As such, KLF5 is a pivotal regulator of the

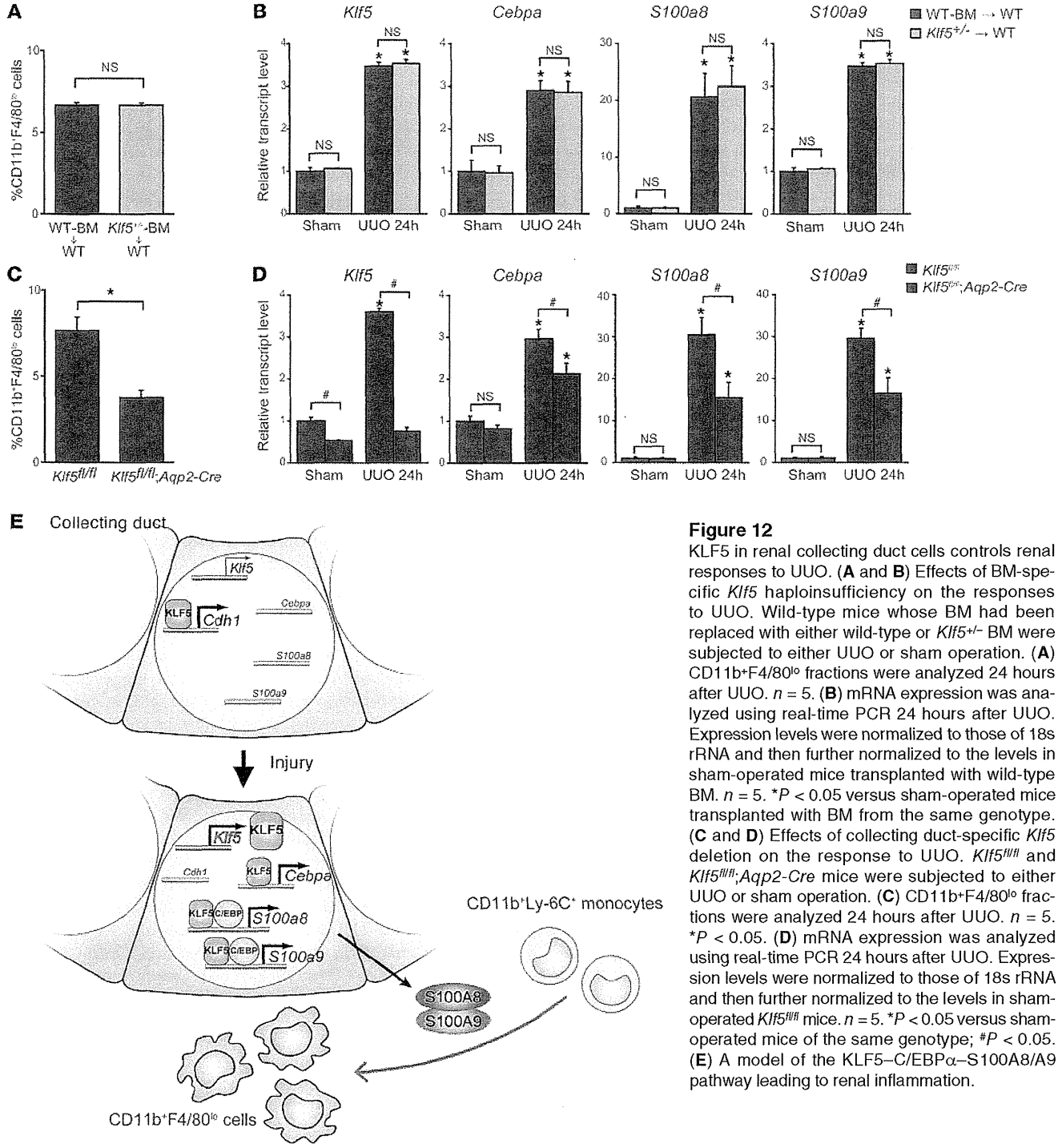

Figure 12

KLF5 in renal collecting duct cells controls renal responses to UUO. (**A** and **B**) Effects of BM-specific *Klf5* haploinsufficiency on the responses to UUO. Wild-type mice whose BM had been replaced with either wild-type or *Klf5*$^{+/-}$ BM were subjected to either UUO or sham operation. (**A**) CD11b^{+}F4/80^{lo} fractions were analyzed 24 hours after UUO. $n = 5$. (**B**) mRNA expression was analyzed using real-time PCR 24 hours after UUO. Expression levels were normalized to those of 18s rRNA and then further normalized to the levels in sham-operated mice transplanted with wild-type BM. $n = 5$. $^{*}P < 0.05$ versus sham-operated mice transplanted with BM from the same genotype. (**C** and **D**) Effects of collecting duct-specific *Klf5* deletion on the response to UUO. *Klf5*$^{fl/fl}$ and *Klf5*$^{fl/fl}$;*Aqp2-Cre* mice were subjected to either UUO or sham operation. (**C**) CD11b^{+}F4/80^{lo} fractions were analyzed 24 hours after UUO. $n = 5$. $^{*}P < 0.05$. (**D**) mRNA expression was analyzed using real-time PCR 24 hours after UUO. Expression levels were normalized to those of 18s rRNA and then further normalized to the levels in sham-operated *Klf5*$^{fl/fl}$ mice. $n = 5$. $^{*}P < 0.05$ versus sham-operated mice of the same genotype; $^{\#}P < 0.05$. (**E**) A model of the KLF5–C/EBPα–S100A8/A9 pathway leading to renal inflammation.

response of collecting duct cells to renal injury. Because KLF5 regulates early accumulation of CD11b^{+}Ly-6C^{lo} cells in UUO kidneys, *Klf5* haploinsufficiency and collecting duct–specific *Klf5* deletion skewed macrophage differentiation toward M2, leading to amelioration of the renal injury but enhancement of the fibrosis.

Our identification of two CD11b^{+}F4/80^{+} cell subpopulations with different gene expression profiles clearly demonstrates that renal inflammation involves at least two phenotypically different monocyte/macrophage subpopulations: CD11b^{+}F4/80^{lo} monocytes/macrophages showing M1-type activation and CD11b^{+}F4/80^{hi} M2-type macrophages. In addition, we found that these subpopulations differentially accumulate over the course of the response to UUO: on days 1–4 after UUO, macrophage activation was skewed to M1-type, but at later times it was shifted toward M2-type. Lin et al. recently identified subsets of macrophages in UUO kidneys based on the surface expression of Ly-6C (11). In

their study, CD11b$^+$Ly-6C^{hi} immature macrophages exhibited M1-type activation, while CD11b$^+$Ly-6C^{lo} macrophages showed the M2-type phenotype. The gene expression profiles and surface phenotypes observed in the present study strongly suggest that CD11b$^+$F4/80^{lo} and CD11b$^+$F4/80^{hi} cells largely correspond to the CD11b$^+$Ly-6C^{hi} and CD11b$^+$Ly-6C^{lo} macrophages, respectively.

The results of the present study demonstrate that renal CD11b$^+$F4/80^{lo} and CD11b$^+$F4/80^{hi} cells differ functionally from one another. By showing that inflammatory CD11b$^+$F4/80^{lo} M1-type cell accumulation was selectively suppressed in *Klf5*$^{+/-}$ mice and that tubular injury, cellular apoptosis, and proinflammatory cytokine expression were all diminished in *Klf5*$^{+/-}$ mice, the present study demonstrates that M1-type macrophages are crucially involved in the renal injury and inflammation caused by UUO. Our results also indicate that CD11b$^+$F4/80^{lo} and CD11b$^+$F4/80^{hi} cells differentially contribute to the renal response to injury, at least in part through production of different sets of cytokines. Interestingly, fibrosis was enhanced in *Klf5*$^{+/-}$ and *Klf5*$^{fl/fl}$;*Aqp2-Cre* mice, in which CD11b$^+$F4/80^{hi} M2-type macrophage accumulation was increased but accumulation of CD11b$^+$F4/80^{lo} M1-type cells was reduced. This suggests that the skewed balance toward M2 activation in *Klf5*$^{+/-}$ mice led to the enhanced fibrosis. Histologically, however, interstitial fibrosis was apparent only on day 7; thereafter, differences in the M1/M2 ratio were no longer observed between wild-type and *Klf5*$^{+/-}$ kidneys (Figure 4B). Nonetheless, expression levels of genes involved in fibrosis, including *Col3a1*, *Fn1*, *Vim*, and *Tgfb1*, were significantly increased from day 4 in *Klf5*$^{+/-}$ kidneys (Figure 3B). The activation of fibrotic processes therefore appears to coincide with increases in the M2-type cell fractions in *Klf5*$^{+/-}$ kidneys. These findings suggest that the renal environment (e.g., skewed balance toward M2 activation, reduced expression of proinflammatory cytokines, and increased expression of TGF-β1) at early times after UUO (up to day 7) alters inflammatory processes and affects the later fibrotic phenotype. This idea is supported by our finding that on day 7 levels of *Il1b* and *Ccl2* expression were reduced in CD11b$^+$F4/80^{lo} cells in *Klf5*$^{+/-}$ kidneys, while levels of *Tgf1b* and *Il10* expression were increased in CD11b$^+$F4/80^{hi} cells (Figure 7). The finding that injection of *Klf5*$^{+/-}$ mice with S100A8 or S100A9 not only skewed the monocyte/macrophage balance toward CD11b$^+$F4/80^{lo} M1-type cells but also suppressed interstitial fibrosis (Supplemental Figure 13) also supports the model.

In earlier studies, the same renal CD11b$^+$ mononuclear cell populations were identified variously as macrophages or DCs. In the present study, we refer to CD11b$^+$F4/80^{hi} cells as macrophages because they clearly differ from classical DCs in the following ways: (a) CD11c levels are lower and F4/80 levels are higher than in classical DCs; (b) CD83 expression is absent; (c) they have a macrophage-like morphology; and (d) they can be differentiated from inflammatory monocytes (11). Similarly, Lin et al. referred to CD11b$^+$Ly-6C^{lo} cells as macrophages (11), though other groups have identified populations of kidney CD11b$^+$ cells as DCs. For example, Li et al. referred to resident CD11b$^+$F4/80^{hi} cells as DCs, based on the intermediate expression of CD11c and other DC markers, including MHCII and CD86 (27). Dong et al. identified CD11c^{int}F4/80$^+$Ly-6C$^-$ cells as F4/80$^+$ DCs and showed that the population is increased in UUO kidneys (42). And Heymann et al. described CD11c^{int}CD11b^{int} cells as resident DCs in mouse glomerulonephritis modes (43). Although the precise relationships between these cells are difficult to define due to a lack of the common reference cells (e.g., spleen cells) and differences in the flow cytometric methods used, CD11b$^+$F4/80^{hi} cells, or at least subpopulations of them, appear to overlap previously identified kidney DCs. It has been difficult to clearly distinguish between macrophages and DCs, as these closely related cells share both phenotypical and functional characteristics particularly during inflammation (44). No single marker can unambiguously distinguish DCs from macrophages, and CD11c, which has been extensively used to identify DCs, is widely expressed in macrophages. Moreover, the capacity to present antigens to T cells, which is a characteristic of DCs, has also been seen in macrophages (31). Consequently, the same cell populations in various tissues have been identified as either DCs or macrophages. In particular, whether CD11c$^+$ cells derived from circulating monocytes should be classified as DCs is a matter of debate (31, 44). In the small intestine, for instance, in addition to CD11c^{hi}CD11b$^+$CD103$^+$CX3CR1$^-$ bona fide DCs, there are Ly-6c^{hi} monocyte-derived CD11c^{int}CD11b$^+$CD103$^-$CX3CR1$^+$ cells, which appear to share at least some phenotypes with renal CD11b$^+$F4/80^{hi} cells (27) and are considered by some researchers to be DCs (34, 45). However, intestinal CX3CR1$^+$ cells do not migrate into draining mesenteric lymph nodes or efficiently present antigens to T cells (46). These characteristics of intestinal CX3CR1$^+$ cells are indistinguishable from those of tissue macrophages (44). Clearly, further study of the lineages and functions, including migratory capacity, of kidney CD11b$^+$ cells will be needed to determine whether they should be classified as macrophages or DCs.

Renal CD11c^{hi}MHCII$^+$CD83$^+$CD11b$^-$ cells closely resemble splenic classical DCs phenotypically and morphologically. An earlier study identified CD11c$^+$CD103$^+$MHCII$^+$CD11b$^-$ cells in kidneys as CD103$^+$ DCs (47), and those cells might be related to the CD11c^{hi} cells identified in the present study. However, additional studies of the function and lineage of these cells will be needed before they can be classified as renal classical DCs.

The surface phenotypes of CD11b$^+$F4/80^{lo} cells (e.g., CD11c^{lo}MHCII$^{-/+}$CD86$^-$CD83$^-$), their morphology, and the fact that they derive from inflammatory monocytes all strongly suggest they are macrophages and monocytes in the process of differentiating into macrophages. However, these cells might also have been identified as inflammatory DCs in some studies (42). In addition, we found that a minor population of CD11b$^+$F4/80^{lo} cells showed higher levels of CD11c and MHCII, particularly in normal and day-7 UUO kidneys (Supplemental Figure 6). Given that inflammatory monocytes can differentiate into CD11b$^+$F4/80^{hi} cells as well as CD11b$^+$F4/80^{lo} cells (Supplemental Figure 12 and ref. 11), they may represent intermediary cells differentiating into CD11b$^+$F4/80^{hi} M2-type cells. Future studies should address the differentiation pathways of inflammatory monocytes within kidneys and identify markers with which to trace them.

S100A8 and S100A9 are calcium-binding secretory proteins that can form homodimers and heterodimers, with the latter being more prevalent (48, 49). We found that levels of *S100a8* and *S100a9* expression peaked on days 1 and 4, respectively, after UUO (Figure 11A), at a time when CD11b$^+$F4/80^{lo} cells were accumulating within the kidneys (Figure 4B), which suggests S100A8 and S100A9 are essential for inflammatory CD11b$^+$F4/80^{lo} cell accumulation early in the response to UUO. We also found that adoptively transferred CD11b$^+$Ly-6C$^+$ inflammatory monocytes were recruited to kidneys following S100A8/A9 injection, and that the recruited cells exhibited the CD11b$^+$F4/80^{lo}Ly-6C$^+$CD206$^-$CD301$^-$ M1-type phenotype (Figure 8C). S100A8 and S100A9 were also capable of inducing M1 markers in BMDMs (Figure 8A). Collectively, these results demon-

strate that S100A8 and S100A9 are important for the recruitment of inflammatory monocytes and their subsequent differentiation into M1-type macrophages during the early response to UUO.

That the accumulation of CD11b$^+$F4/80^{hi} cells begins 4 days after UUO suggests the renal microenvironment only becomes supportive of M2 activation at later times. Consistent with this idea, we found that only a minor population of CD11b$^+$Ly-6C$^+$ monocytes acquires the M2-type phenotype when transferred prior to UUO, whereas Lin et al. showed that when transferred 5 days after UUO, major populations of CD11b$^+$Ly-6C$^+$ monocytes exhibit the M2-type phenotype (11). Because S100A8/A9 expression declines, it is likely that other cytokines recruit monocytes to kidneys at later times after UUO. MCP-1 (CCL2) is one candidate chemokine for such later recruitment (Figure 11A). Although we favor a model in which proinflammatory monocytes differentiate into at least two types of macrophages in response to the kidney microenvironment, the fact that monocytes appear to be recruited by different signals at different times suggests there are multiple subsets CD11b$^+$Ly-6C$^+$ inflammatory monocytes that are differentially recruited to kidneys and might differ in the direction of their differentiation (25).

The results obtained with *Klf5$^{fl/fl}$;Aqp2-Cre* mice demonstrate that expression of KLF5 in collecting duct epithelial cells is essential for the renal response to UUO. However, KLF5 might also have functions in other cell types, including macrophages and fibroblasts. Results obtained after transplantation of *Klf5$^{+/-}$* BM and in *Klf5$^{fl/fl}$;LysM-Cre* mice indicate that, even if KLF5 were functionally active in macrophages, its cell-autonomous function in macrophages would not be important for the renal *Klf5$^{+/-}$* phenotypes. Indeed, the reduced expression of *Il1b* and *Ccl2* in CD11b$^+$F4/80^{lo} cells and increased expression of *Tgfb1* and *Il10* in CD11b$^+$F4/80^{hi} cells in *Klf5$^{+/-}$* mice, but not *Klf5$^{fl/fl}$;LysM-Cre* mice (Figure 7, A and B), is indicative of the importance of cell non-cell-autonomous effects on macrophage activation in *Klf5$^{+/-}$* kidneys. Fibroblasts are another important cell type involved in mediating tubulointerstitial damage, and we previously showed that KLF5 expressed in cardiac fibroblasts is important for the cardiac responses to pressure overload (18). In kidneys the level of *Klf5* expression in α-SMA$^+$ myofibroblasts, mesangial cells, and smooth muscle cells was significantly lower than in cardiac fibroblasts (Supplemental Figure 1C). Moreover, if the functions of KLF5 in renal fibroblasts are similar to those in cardiac fibroblasts, *Klf5* haploinsufficiency in renal fibroblasts would reduce fibrosis. It is therefore unlikely that cell-autonomous alterations of fibroblast function due to *Klf5* haploinsufficiency make a major contribution to the renal *Klf5$^{+/-}$* phenotypes. The results of the present study thus indicate that the observed renal *Klf5$^{+/-}$* phenotypes primarily reflect *Klf5* haploinsufficiency in the collecting duct.

Our data show that collecting duct epithelial cells are the major sensor of stress elicited by UUO. One important question remaining is, what do those cells sense? Given that *Klf5* expression was increased within 4 hours after UUO, and KLF5 bound to the *S100a8* and *S100a9* promoters within 12 hours, at a time when structural changes were minimal, it is very unlikely that pelvic dilation is the cause. One attractive candidate is mechanical force. After UUO there is a sudden rise in ureteric and intrarenal pressure, which translates into tubular mechanical stretch (50). Although very little is known about the effects of mechanical stretch on collecting duct epithelial cells, mechanical stretch is known to profoundly affect the function in various cell types (51). On the other hand, many other factors, including proteinuria, hypoxia, oxidative stress, and glomerulus-derived cytokines, likely contribute to activation of collecting duct cells (3). In that regard, we recently found that reactive oxygen species induce *Klf5* expression in smooth muscle cells (52). Much work will be needed to clarify the mechanism by which collecting duct epithelial cells are activated under various disease conditions. Nevertheless, the results of the present study clearly indicate that the collecting duct is an essential regulator of inflammatory processes in the kidney, and the molecular mechanism identified in the present study may provide attractive targets for novel therapeutic strategies.

Methods

Mice. Male C57BL6/6J mice were purchased from CLEA Japan and maintained on a standard mouse chow diet. *Klf5$^{+/-}$* and *Klf5$^{fl/fl}$* mice were generated as described previously (17, 18). *Aqp2-Cre* mice were purchased from The Jackson Laboratory. UUO was performed as described previously (53). For BM transplantation, 8-week-old mice were lethally irradiated, and the next day unfractionated BM cells were administered to each recipient mouse. See Supplemental Methods for details. For renal function analysis, reversible UUO was performed (22). Briefly, 12-week-old mice were anesthetized and the right ureter was then ligated. After 3 days the right ureter ligation was removed, and the mice were allowed to recover for 7 days before the left ureter was ligated. All experiments were approved by the University of Tokyo Ethics Committee for Animal Experiments and strictly adhered to the guidelines for animal experiments of the University of Tokyo.

Flow cytometric analysis. The methods used to prepare cells from kidneys were described previously (54). All flow cytometric analyses were performed using a FACScalibur (BD) and FlowJo software (Tree Star). Cells were sorted using a FACSaria II (BD). See Supplemental Methods for details.

ChIP assays. ChIP assays were carried out as described previously (19). ChIP-seq was performed by sequencing the immunoprecipitated DNA using a 454 sequencer (Roche Diagnostics), after which the sequence reads were mapped to the reference mouse genome. See Supplemental Methods for details of in vivo ChIP and re-ChIP assays.

Infusion of recombinant proteins into kidney. Human recombinant S100A8 and A100A9 were purchased from ProtEra and dissolved in PBS (0.5 mg/ml). The LPS level in the mixed S100A8 and S100A9 solution was analyzed using a limulus amoebocyte lysate assay (Seikagaku Biobusiness Corp.). As solution of LPS in PBS in which the LPS concentration was matched to that in the S100A8/A9 solution (0.092 EU/ml) served as a control. An isotonic solution of glucose in PBS and PBS alone were also used as controls. A mixture of S100A8 and S100A9 (25 μg each) was injected into the parenchyma of the left kidney without vascular clamping. The total injected volume for one kidney was 50 μl.

Statistics. Comparisons between 2 groups were made using Student's *t* test (2-tailed). Differences among more than 2 groups were analyzed using 1-way ANOVA followed by Bonferroni (3 groups) or Tukey-Kramer post hoc (>4 groups) tests. *P* values less than 0.05 were considered significant. Error bars represent SD except where otherwise indicated.

Acknowledgments

We gratefully acknowledge M. Hayashi, N. Yamanaka, A. Ono, X. Yingda, Y. Tani, and E. Magoshi for their excellent technical assistance. We would like to thank Carey Lumeng for valuable discussion. This study was supported in part by the Funding Program for World-Leading Innovative R&D on Science and Technology (FIRST Program) from the Japan Society for the Promotion of Science (to R. Nagai); grants-in-aid from the Ministry of Education, Culture, Sports, Science and Technology, Japan (to R. Nagai, I. Manabe, and

K. Fujiu); a grant for Translational Systems Biology and Medicine Initiative from the Ministry of Education, Culture, Sports, Science and Technology of Japan and a research grant from the National Institute of Biomedical Innovation (to R. Nagai); and research grants from the Japan Science and Technology Institute, the Sumitomo Foundation, Takeda Science Foundation, the Mochida Memorial Foundation for Medical and Pharmaceutical Research, and the Mitsubishi Pharma Research Foundation (to I. Manabe).

Received for publication February 14, 2011, and accepted in revised form June 8, 2011.

Address correspondence to: Ichiro Manabe or Ryozo Nagai, Department of Cardiovascular Medicine, University of Tokyo, 7-3-1, Hongo, Bunkyo, Tokyo 113-8655, Japan. Phone: 81.3.3815.6672; Fax: 81.3.3818.6673; E-mail: manabe-tky@umin.ac.jp (I. Manabe), nagai-tky@umin.ac.jp (R. Nagai).

1. Harris RC, Neilson EG. Toward a unified theory of renal progression. *Annu Rev Med.* 2006;57:365–380.
2. Chevalier RL, Forbes MS, Thornhill BA. Ureteral obstruction as a model of renal interstitial fibrosis and obstructive nephropathy. *Kidney Int.* 2009;75(11):1145–1152.
3. Sean Eardley K, Cockwell P. Macrophages and progressive tubulointerstitial disease. *Kidney Int.* 2005;68(2):437–455.
4. Schnaper HW, Kopp JB. Why kidneys fail: report from an American Society of Nephrology advances in research conference. *J Am Soc Nephrol.* 2006; 17(7):1777–1781.
5. Kluth DC, Erwig L-P, Rees AJ. Multiple facets of macrophages in renal injury. *Kidney Int.* 2004;66(2):542–557.
6. Ricardo SD, van Goor H, Eddy AA. Macrophage diversity in renal injury and repair. *J Clin Invest.* 2008;118(11):3522–3530.
7. Kluth DC. Pro-resolution properties of macrophages in renal injury. *Kidney Int.* 2007;72(3):234–236.
8. Duffield JS, et al. Selective depletion of macrophages reveals distinct, opposing roles during liver injury and repair. *J Clin Invest.* 2005;115(1):56–65.
9. Mosser DM, Edwards JP. Exploring the full spectrum of macrophage activation. *Nat Rev Immunol.* 2008;8(12):958–969.
10. Mantovani A. Macrophage diversity and polarization: in vivo veritas. *Blood.* 2006;108(2):408–409.
11. Lin SL, Castano AP, Nowlin BT, Lupher ML Jr, Duffield JS. Bone marrow Ly6Chigh monocytes are selectively recruited to injured kidney and differentiate into functionally distinct populations. *J Immunol.* 2009;183(10):6733–6743.
12. Fenton RA, Knepper MA. Mouse models and the urinary concentrating mechanism in the new millennium. *Physiol Rev.* 2007;87(4):1083–1112.
13. Ivanova L, Butt MJ, Matsell DG. Mesenchymal transition in kidney collecting duct epithelial cells. *Am J Physiol Renal Physiol.* 2008;294(5):F1238–F1248.
14. Smith JP, Pozzi A, Dhawan P, Singh AB, Harris RC. Soluble HB-EGF induces epithelial-to-mesenchymal transition in inner medullary collecting duct cells by upregulating Snail-2. *Am J Physiol Renal Physiol.* 2009;296(5):F957–F965.
15. Butt MJ, Tarantal AF, Jimenez DF, Matsell DG. Collecting duct epithelial-mesenchymal transition in fetal urinary tract obstruction. *Kidney Int.* 2007;72(8):936–944.
16. Haldar SM, Ibrahim OA, Jain MK. Kruppel-like factors (KLFs) in muscle biology. *J Mol Cell Cardiol.* 2007;43(1):1–10.
17. Shindo T, et al. Kruppel-like zinc-finger transcription factor KLF5/BTEB2 is a target for angiotensin II signaling and an essential regulator of cardiovascular remodeling. *Nat Med.* 2002;8(8):856–863.
18. Takeda N, et al. Cardiac fibroblasts are essential for the adaptive response of the murine heart to pressure overload. *J Clin Invest.* 2010;120(1):254–265.
19. Fujiu K, et al. Synthetic retinoid Am80 suppresses smooth muscle phenotypic modulation and in-stent neointima formation by inhibiting KLF5. *Circ Res.* 2005;97(11):1132–1141.
20. Nelson RD, et al. Expression of an AQP2 Cre recombinase transgene in kidney and male reproductive system of transgenic mice. *Am J Physiol Cell Physiol.* 1998;275(1 pt 1):C216–C226.
21. Bascands JL, Schanstra JP. Obstructive nephropathy: insights from genetically engineered animals. *Kidney Int.* 2005;68(3):925–937.
22. Puri TS, et al. Chronic kidney disease induced in mice by reversible unilateral ureteral obstruction is dependent on genetic background. *Am J Physiol Renal Physiol.* 2010;298(4):F1024–F1032.
23. Medzhitov R. Origin and physiological roles of inflammation. *Nature.* 2008;454(7203):428–435.
24. Zhu B, et al. CD11b+Ly-6C(hi) suppressive monocytes in experimental autoimmune encephalomyelitis. *J Immunol.* 2007;179(8):5228–5237.
25. Swirski FK, et al. Ly-6Chi monocytes dominate hypercholesterolemia-associated monocytosis and give rise to macrophages in atheromata. *J Clin Invest.* 2007;117(1):195–205.
26. Geissmann F, Manz MG, Jung S, Sieweke MH, Merad M, Ley K. Development of monocytes, macrophages, and dendritic cells. *Science.* 2010;327(5966):656–661.
27. Li L, et al. The chemokine receptors CCR2 and CX3CR1 mediate monocyte/macrophage trafficking in kidney ischemia-reperfusion injury. *Kidney Int.* 2008;74(12):1526–1537.
28. Krüger T, et al. Identification and functional characterization of dendritic cells in the healthy murine kidney and in experimental glomerulonephritis. *J Am Soc Nephrol.* 2004;15(3):613–621.
29. Dong X, Swaminathan S, Bachman LA, Croatt AJ, Nath KA, Griffin MD. Resident dendritic cells are the predominant TNF-secreting cell in early renal ischemia-reperfusion injury. *Kidney Int.* 2007;71(7):619–628.
30. Hochheiser K, Tittel A, Kurts C. Kidney dendritic cells in acute and chronic renal disease. *Int J Exp Pathol.* 2011;92(3):193–201.
31. Hume DA. Macrophages as APC and the dendritic cell myth. *J Immunol.* 2008;181(9):5829–5835.
32. Prechtel A, Steinkasserer A. CD83: an update on functions and prospects of the maturation marker of dendritic cells. *Arch Dermatol Res.* 2007;299(2):59–69.
33. Vakkila J, Lotze MT, Riga C, Jaffe R. A basis for distinguishing cultured dendritic cells and macrophages in cytospins and fixed sections. *Pediatr Dev Pathol.* 2005;8(1):43–51.
34. Pabst O, Bernhardt G. The puzzle of intestinal lamina propria dendritic cells and macrophages. *Eur J Immunol.* 2010;40(8):2107–2111.
35. Liu Y, et al. Unique expression of suppressor of cytokine signaling 3 is essential for classical macrophage activation in rodents in vitro and in vivo. *J Immunol.* 2008;180(9):6270–6278.
36. Vandal K, Rouleau P, Boivin A, Ryckman C, Talbot M, Tessier PA. Blockade of S100A8 and S100A9 suppresses neutrophil migration in response to lipopolysaccharide. *J Immunol.* 2003;171(5):2602–2609.
37. Ryckman C, Vandal K, Rouleau P, Talbot M, Tessier PA. Proinflammatory activities of S100: proteins S100A8, S100A9, and S100A8/A9 induce neutrophil chemotaxis and adhesion. *J Immunol.* 2003;170(6):3233–3242.
38. Endoh Y, Chung YM, Clark IA, Geczy CL, Hsu K. IL-10-dependent S100A8 gene induction in monocytes/macrophages by double-stranded RNA. *J Immunol.* 2009;182(4):2258–2268.
39. Nacken W, Lekstrom-Himes JA, Sorg C, Manitz MP. Molecular analysis of the mouse S100A9 gene and evidence that the myeloid specific transcription factor C/EBPepsilon is not required for the regulation of the S100A9/A8 gene expression in neutrophils. *J Cell Biochem.* 2001;80(4):606–616.
40. Kuwayama A, Kuruto R, Horie N, Takeishi K, Nozawa R. Appearance of nuclear factors that interact with genes for myeloid calcium binding proteins (MRP-8 and MRP-14) in differentiated HL-60 cells. *Blood.* 1993;81(11):3116–3121.
41. Clausen BE, Burkhardt C, Reith W, Renkawitz R, Förster I. Conditional gene targeting in macrophages and granulocytes using LysMcre mice. *Transgenic Res.* 1999;8(4):265–277.
42. Dong X, Bachman LA, Miller MN, Nath KA, Griffin MD. Dendritic cells facilitate accumulation of IL-17 T cells in the kidney following acute renal obstruction. *Kidney Int.* 2008;74(10):1294–1309.
43. Heymann F, et al. Kidney dendritic cell activation is required for progression of renal disease in a mouse model of glomerular injury. *J Clin Invest.* 2009;119(5):1286–1297.
44. Geissmann F, Gordon S, Hume DA, Mowat AM, Randolph GJ. Unravelling mononuclear phagocyte heterogeneity. *Nat Rev Immunol.* 2010;10(6):453–460.
45. Varol C, et al. Intestinal lamina propria dendritic cell subsets have different origin and functions. *Immunity.* 2009;31(3):502–512.
46. Schulz O, et al. Intestinal CD103+, but not CX3CR1+, antigen sampling cells migrate in lymph and serve classical dendritic cell functions. *J Exp Med.* 2009;206(13):3101–3114.
47. Ginhoux F, et al. The origin and development of nonlymphoid tissue CD103+ DCs. *J Exp Med.* 2009;206(13):3115–3130.
48. Nacken W, Roth J, Sorg C, Kerkhoff C. S100A9/S100A8: myeloid representatives of the S100 protein family as prominent players in innate immunity. *Microsc Res Tech.* 2003;60(6):569–580.
49. Gebhardt C, Németh J, Angel P, Hess J. S100A8 and S100A9 in inflammation and cancer. *Biochem Pharmacol.* 2006;72(11):1622–1631.
50. Quinlan MR, Docherty NG, Watson RWG, Fitzpatrick JM. Exploring mechanisms involved in renal tubular sensing of mechanical stretch following ureteric obstruction. *Am J Physiol Renal Physiol.* 2008;295(1):F1–F11.
51. Jaalouk DE, Lammerding J. Mechanotransduction gone awry. *Nat Rev Mol Cell Biol.* 2009;10(1):63–73.
52. Oishi Y, et al. Regulatory polymorphism in transcription factor KLF5 at the MEF2 element alters the response to angiotensin II and is associated with human hypertension. *FASEB J.* 2010; 24(6):1780–1788.
53. Ophascharoensuk V, et al. Obstructive uropathy in the mouse: role of osteopontin in interstitial fibrosis and apoptosis. *Kidney Int.* 1999;56(2):571–580.
54. Vielhauer V, Anders HJ, Perez de Lema G, Luckow B, Schlondorff D, Mack M. Phenotyping renal leukocyte subsets by four-color flow cytometry: characterization of chemokine receptor expression. *Nephron Exp Nephrol.* 2003;93(2):e63.

Cell Stem Cell
Resource

Distinct Metabolic Flow Enables Large-Scale Purification of Mouse and Human Pluripotent Stem Cell-Derived Cardiomyocytes

Shugo Tohyama,[1,3] Fumiyuki Hattori,[1,4,*] Motoaki Sano,[1] Takako Hishiki,[2] Yoshiko Nagahata,[2,5] Tomomi Matsuura,[2,5] Hisayuki Hashimoto,[1] Tomoyuki Suzuki,[6] Hiromi Yamashita,[1,4] Yusuke Satoh,[1] Toru Egashira,[1] Tomohisa Seki,[1] Naoto Muraoka,[1] Hiroyuki Yamakawa,[1] Yasuyuki Ohgino,[1] Tomofumi Tanaka,[4] Masatoshi Yoichi,[4] Shinsuke Yuasa,[1] Mitsushige Murata,[1] Makoto Suematsu,[2,5] and Keiichi Fukuda[1,*]
[1]Department of Cardiology
[2]Department of Biochemistry
Keio University School of Medicine, Tokyo 160-8582, Japan
[3]Japan Society for the Promotion of Science, Tokyo 102-8472, Japan
[4]Asubio Pharma, Kobe 650-0047, Japan
[5]Japan Science and Technology Agency (JST), Exploratory Research for Advanced Technology (ERATO) Suematsu Gas Biology Project, Tokyo 160-8582, Japan
[6]Department of Cardiovascular Research, Research Institute of Environmental Medicine, Nagoya University, Nagoya 464-8601, Japan
*Correspondence: hattori.fumiyuki.ef@asubio.co.jp (F.H.), kfukuda@a2.keio.jp (K.F.)
http://dx.doi.org/10.1016/j.stem.2012.09.013

SUMMARY

Heart disease remains a major cause of death despite advances in medical technology. Heart-regenerative therapy that uses pluripotent stem cells (PSCs) is a potentially promising strategy for patients with heart disease, but the inability to generate highly purified cardiomyocytes in sufficient quantities has been a barrier to realizing this potential. Here, we report a nongenetic method for mass-producing cardiomyocytes from mouse and human PSC derivatives that is based on the marked biochemical differences in glucose and lactate metabolism between cardiomyocytes and noncardiomyocytes, including undifferentiated cells. We cultured PSC derivatives with glucose-depleted culture medium containing abundant lactate and found that only cardiomyocytes survived. Using this approach, we obtained cardiomyocytes of up to 99% purity that did not form tumors after transplantation. We believe that our technological method broadens the range of potential applications for purified PSC-derived cardiomyocytes and could facilitate progress toward PSC-based cardiac regenerative therapy.

INTRODUCTION

Heart disease is a common and deadly disease, and heart-regenerative therapy is a promising therapeutic strategy for some patients (Passier et al., 2008). Pluripotent stem cells (PSCs) including embryonic stem cells (ESCs) and induced pluripotent stem cells (iPSCs) are potential sources for production of therapeutic cardiomyocytes (Burridge et al., 2012; Takahashi et al., 2007; Thomson et al., 1998). A typical human left ventricle contains roughly 6×10^9 cardiomyocytes; thus, nearly 1×10^9 de novo cardiomyocytes would be required per patient for this type of repair (Hattori and Fukuda, 2012). However, PSC-based approaches carry a high risk of tumor formation due to contamination of residual PSCs in the therapeutic cell preparations. Therefore, obtaining highly purified cardiomyocytes will be key for achieving therapeutic success in applying these cells.

Procedures involving density-gradient centrifugation (Laflamme et al., 2007; Xu et al., 2006), genetic modification (Fijnvandraat et al., 2003; Gassanov et al., 2004; Hidaka et al., 2003; Klug et al., 1996), and nongenetic methods that use a mitochondrial dye (Hattori et al., 2010) or antibodies to specific cell-surface markers (Dubois et al., 2011; Uosaki et al., 2011) have been established for cardiomyocyte enrichment. However, none of these methods are ideal for the therapeutic application of PSC-derived cardiomyocytes because of drawbacks including insufficient purity, genotoxicity, and the use of fluorescence-activated cell sorting (FACS) and/or antibodies.

Glucose is the main source of energy and anabolic precursors in various mammalian cells. It is converted by glycolysis into pyruvate and/or lactate via glucose-6-phosphate (G6P; a source of nucleotides) and 3-phosphoglycerate (a source of some amino acids) for generation of two ATP molecules without the need for oxygen. Pyruvate is further utilized in the mitochondrial tricarboxylic acid (TCA) cycle for production of 36 ATP molecules via oxidative phosphorylation (OXPHOS). Cardiomyocytes efficiently produce energy from several substrates including glucose, fatty acids, and lactate via OXPHOS. Interestingly, there are marked changes between energy substrate utilization by cardiomyocytes before and after birth. The fetal heart has a higher capacity for lactate uptake than the adult heart (Fisher et al., 1981) and uses lactate as a major energy source (Neely and Morgan, 1974; Werner and Sicard, 1987) by exploiting the lactate-rich environment created by the placenta (Burd et al., 1975).

In this study, we took advantage of the unique metabolic properties of cardiomyocytes to develop an efficient and

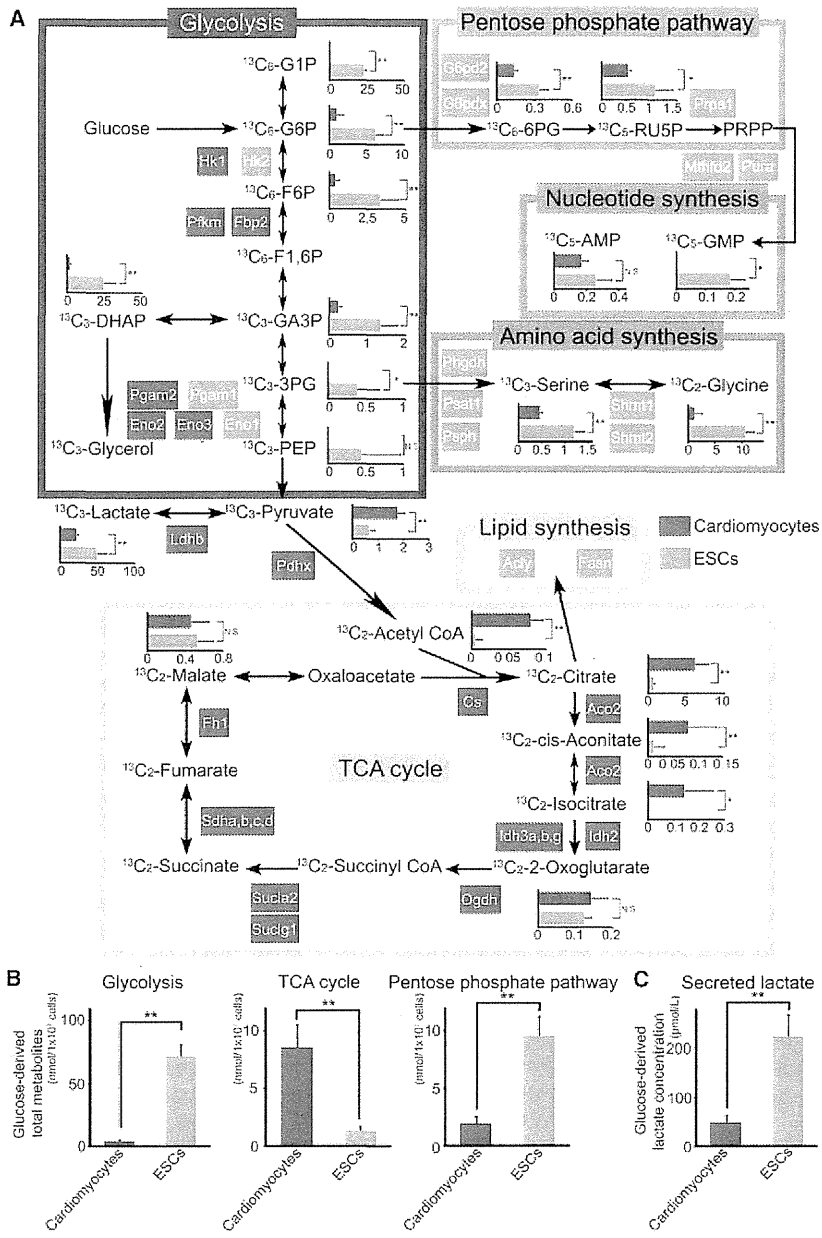

Figure 1. Distinct Metabolic Differences Between Cardiomyocytes and ESCs in Transcriptome and Fluxome Analyses

(A) Metabolic pathway map summarizing the results from gene array and [^{13}C]-labeled glucose fluxome analyses. Gene names shown in red or blue boxes indicate the mRNA expression levels increased more than 2-fold in cardiomyocytes or ESCs, respectively. The bar graphs represent the detected levels of [^{13}C]-labeled metabolites in cardiomyocytes (red bar) and ESCs (blue bar) (n = 4). All units are nmol per 1.0×10^7 cells. All data were obtained from independent experiments.

(B) Total [^{13}C]-labeled metabolites of cardiomyocytes (red bar) and ESCs (blue bar) in each key pathway (n = 4).

(C) Secreted [^{13}C]-labeled lactate concentration in the media of cardiomyocytes (red bar) and ESCs (blue bar) (n = 4). All data were obtained from independent experiments.

*$p < 0.05$; **$p < 0.01$. Data are shown as mean ± SD. All the abbreviations are shown in Table S1. See also Figure S1 and Table S1.

noninvasive environmental approach for their purification from PSC cultures.

RESULTS

Integrated Transcriptomic and Metabolomic Analyses Highlight Distinct Metabolic Differences between Cardiomyocytes and Other Proliferating Cells

To find metabolism-related genes that are differentially expressed between undifferentiated stem cells and cardiomyocytes, we performed comparative transcriptome analyses of undifferentiated mouse ESCs and neonatal mouse cardiomyocytes purified by the "mitochondrial method"(Hattori et al., 2010) (Figures S1A and S1B available online). The results for cardiomyocytes revealed markedly higher expression of genes encoding enzymes involved in the TCA cycle than the undifferentiated ESCs and, in turn, lower expression of genes involved in the pentose phosphate, amino acid synthesis, and lipid synthesis pathways (Figure 1A and Table S1). Next, we conducted a fluxome analysis (Kinoshita et al., 2007; Shintani et al., 2009) to trace a range of metabolites derived from [^{13}C]-labeled glucose in neonatal rat cardiomyocytes, mouse ESCs, a hepatocyte cell line (HepG2), and a skeletal myoblast cell line (C2C12). [^{13}C]-labeled intermediate metabolites of the glycolytic, pentose phosphate, and amino acid synthesis pathways were subsequently found at higher levels in ESCs, HepG2, and C2C12 cells than in cardiomyocytes (Figures 1A, 1B, and S1C and Table S1). ESCs, HepG2, and C2C12 cells also discarded more lactate than cardiomyocytes did (Figure 1C and Figure S1D). In contrast, cardiomyocytes took up pyruvate into mitochondria, and most [^{13}C]-labeled intermediate metabolites of the TCA cycle were significantly higher in cardiomyocytes than in ESCs (Figure 1A). These transcriptome and fluxome analyses highlighted a dynamic difference in the metabolic fates of lactate between cell types (Figure S1E). More specifically, lactate was discarded by noncardiomyocytes but preferentially used in TCA metabolism by cardiomyocytes. We hypothesized that cells mainly dependent on glycolysis might not be able to survive under glucose-depleted and lactate-abundant conditions, whereas cardiomyocytes would survive by using lactate as an alternative energy source.

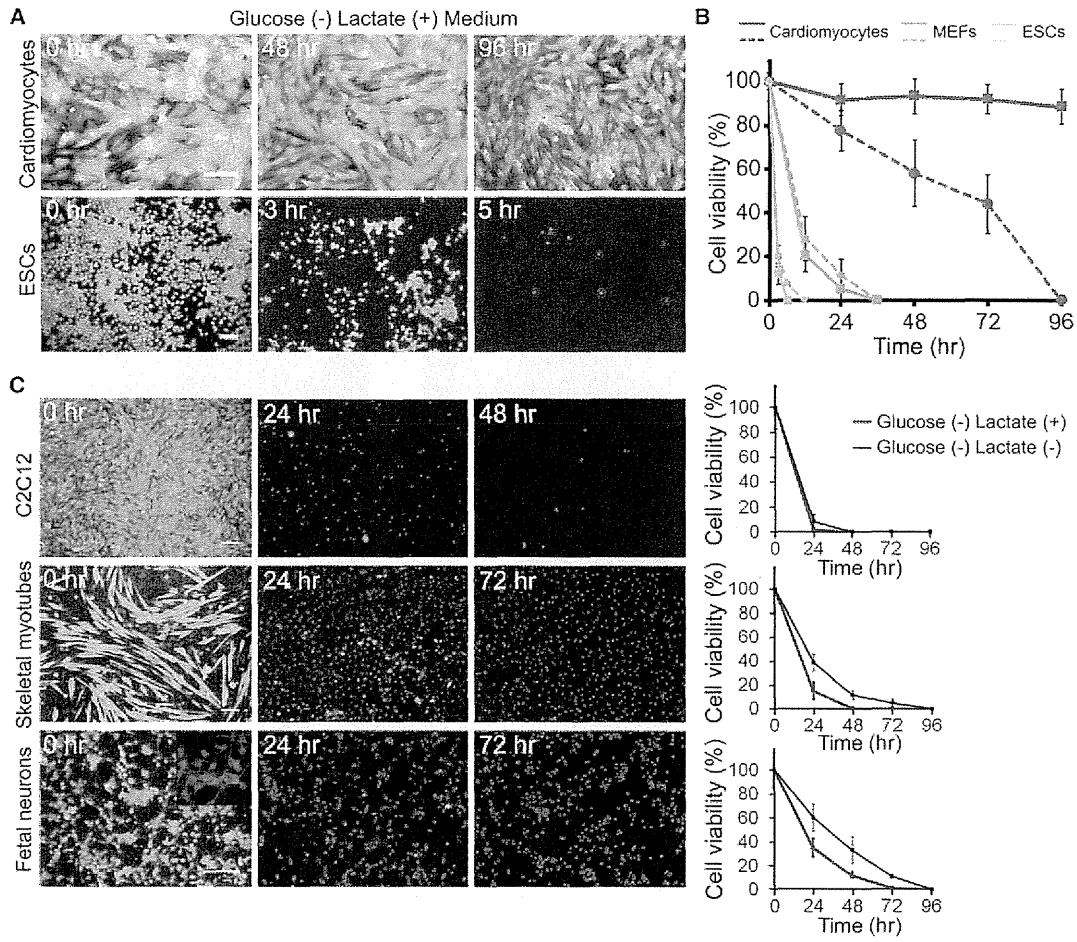

Figure 2. Cell Viabilities of Various Cells under Glucose-Depleted and Lactate-Supplemented Conditions

(A) Cultured neonatal rat cardiomyocytes and mouse ESCs were exposed to glucose-depleted media supplemented with lactate, and their viabilities were assessed with the LIVE/DEAD kit, which indicates viable cells with green fluorescence and dead cells with nuclear red fluorescence.

(B) Time course of viability in neonatal rat cardiomyocytes (red), mouse ESCs (blue), and MEFs (green) under glucose-free conditions with and without lactate (n = 6). Solid lines indicate the glucose-free and lactate-supplemented condition, and dashed lines indicate the glucose-free without lactate condition. All data were obtained from independent experiments.

(C) Noncardiomyocytes including C2C12, skeletal myotubes, and primary cultured neurons were exposed to glucose-free conditions with and without lactate, and their viabilities were assessed with the LIVE/DEAD kit. The time courses of viability were plotted in the line graphs (right) (all cells; n = 4). Red lines indicate the glucose-free and lactate-supplemented condition, and black lines indicate the glucose-free without lactate condition. The inset in primary neurons represents immunocytochemical staining with an antibody to βIII-tubulin (red) and with DAPI (blue).

Scale bars represent 100 μm (A and C). Data are shown as mean ± SD. See also Figure S2.

Glucose-Depleted and Lactate-Enriched Culture Conditions Can Purify Cardiomyocytes from Mouse and Human PSC Derivatives

To test our hypothesis, we exposed neonatal rat cardiomyocytes, mouse ESCs, primary peripheral lymphatic cells, primary fetal neurons, primary mouse embryonic fibroblasts (MEFs), C2C12 cells (myoblasts and myotubes), hepatocytes (HepG2), and renal cells (HEK293) to glucose-depleted conditions with and without various concentrations of lactate. Every type of cell died within 96 hr in the glucose-depleted conditions, and as expected, supplementation with lactate only prolonged the survival of cardiomyocytes (Figures 2A, 2B, 2C and S2). We named this special culture condition for the growth of cardiomyocytes the "lactate method."

We next applied the lactate method to purifying human PSC-derived cardiomyocytes. First, we optimized the time course of the method for human ESC (hESC)-derived cardiomyocytes. Using time-lapse imaging, we observed that 7 days' exposure of hESC- and human iPSC (hiPSC)-derived attached embryoid bodies (EBs) to glucose-free conditions supplemented with 4 mM lactate selectively enriched for beating cells (Movie S1). Second, we confirmed that days 7–8 of culture were the best time points for harvesting the cells, as shown in Figure 3A. To optimize the lactate concentration, we measured the viability

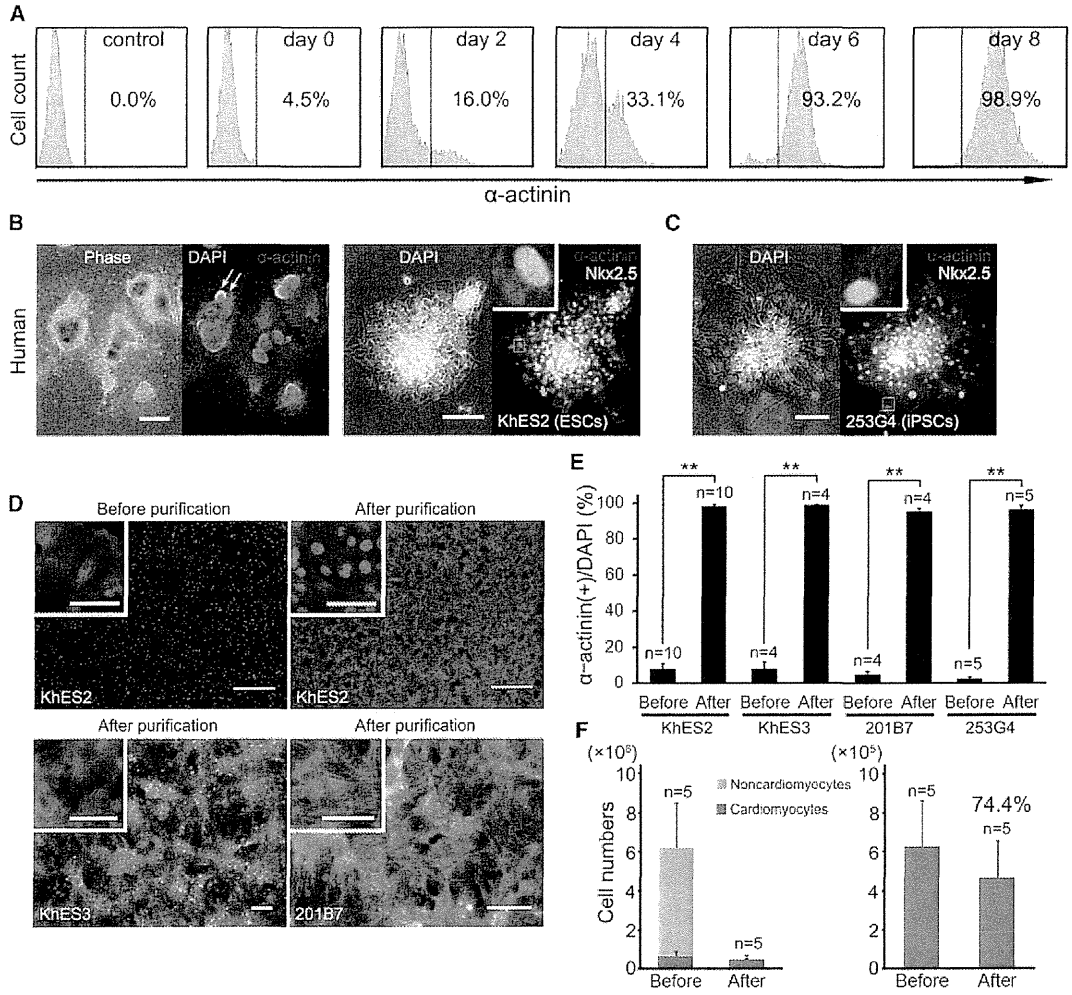

Figure 3. Purification of Cardiomyocytes under Glucose-Depleted and Lactate-Supplemented Conditions

(A) Representative FACS analyses for α-actinin expression in the hESC-derived cells during metabolic selection. Control indicates hESC-derived cells after 2 days of differentiation that do not contain any cardiomyocytes.

(B and C) Representative phase-contrast and immunofluorescent staining for α-actinin in the nonpurified hESC-derived EBs (B, left) and for α-actinin and Nkx2.5 in purified hESC (KhES-2)-derived cardiomyocytes (hESC-CMs) (B, right) and purified hiPSC (253G4)-derived cardiomyocytes (hiPSC-CMs) (C). Arrows indicate α-actinin-positive cells.

(D) Representative immunofluorescent staining for α-actinin (red) in the hESC (KhES-2 and KhES-3)- and hiPSC (201B7)-derived dispersed cells before (upper left) and after (upper right, lower panels) metabolic selection. The cell nuclei are stained by DAPI (blue).

(E) Percentage of α-actinin-positive cardiomyocytes in the hESC (KhES-2 and KhES-3)- and hiPSC (201B7 and 253G4)-derived dispersed cells before and after metabolic selection. All data were obtained from independent experiments.

(F) Numbers of α-actinin-negative noncardiomyocytes (green) and α-actinin-positive cardiomyocytes (red) in the hESC-derived dispersed cells before (n = 5) and after (n = 5) metabolic selection (left graph). The right graph represents only α-actinin-positive cardiomyocytes. All data were obtained from independent experiments.

Scale bars represent 50 μm (D, insets), 100 μm (B, right; C and D, lower panels), and 500 μm (B, left; D, upper panels). $^{**}p < 0.01$. Data are shown as mean ± SD. See also Figure S3 and Movies S1, S2, and S3.

of purified hESC-derived cardiomyocytes exposed to glucose-depleted conditions with various concentrations of lactate for 6 days; we found the lowest numbers of dead cells in 4 mM lactate (Figure S3A). We further tested for the ideal period of differentiation using the lactate method and found that 20–30 days of differentiation produced the highest reproducibility, purity, and yield of cardiomyocytes. To determine why this period is optimal, we investigated the proliferative activity of EBs on various differentiation days (days 14–60) using a 5-ethynyl-20-deoxyuridine (EdU) incorporation assay. The percentage of EdU-incorporated cells markedly decreased after day 30 (Figure S3B), implying that proliferating cells are sensitive to the lactate method. The optimized condition efficiently enriched for globally contracting aggregates in a time-dependent manner (Figure S3C and Movie S2). Concomitantly, messenger RNA (mRNA) expression of the cardiomyocyte-related gene

MYH6 increased, while that of the pluripotency-related gene *POU5F1* (Figure S3D) decreased abruptly. In addition, the mRNAs for noncardiac genes (*NANOG*, *MYOD*, *AFP*, and *MAP2*) were completely eliminated, and those for other cardiomyocyte-related genes (*ACTC1* and *NKX2.5*) were significantly enriched (Figures S3E and S3F). We also observed clumps of purified cardiomyocytes in the adhered condition (Figures 3B and 3C). We dispersed the clumps and cultured the cells therein and then evaluated their purity before and after metabolic selection. The percentages of α-actinin-positive cells before and after metabolic selection were 8.1 ± 2.9% (n = 10) and 98.3 ± 0.9% (n = 10), respectively (Figures 3D and 3E). We also confirmed the efficacy of the lactate method using other hESC (KhES-3) and hiPSC (201B7 and 253G4) lines. As shown in Figures 3D and 3E, the purities were determined as 98.9 ± 0.3, 95.5 ± 1.3, and 96.5 ± 2.0%, respectively. To identify selective events in KhES-2 and iPSCs (253G4 and 201B7), we obtained global gene-expression patterns for the PSC-derived EBs and purified hESC-derived cardiomyocytes. We categorized the expressed genes following the gene ontology consortium and found both similarities and differences among EBs derived from three cell lines (Ashburner et al., 2000). One possible explanation for the differences is that the derived EBs contain various types of cells that are eventually eliminated by the lactate-purification method (Figures S3G and S3H). In our system, 4.0×10^6 hESCs differentiated into $6.2 \pm 2.5 \times 10^6$ (n = 5) cells containing $6.3 \pm 2.3 \times 10^5$ (n = 5) α-actinin-positive cardiomyocytes, and $4.7 \pm 1.8 \times 10^5$ (n = 5) α-actinin-positive cardiomyocytes were finally purified via the lactate method. Therefore, the yield-based efficiency of our lactate method for hESCs was 74.4 ± 12.1% (Figure 3F). To directly compare the yield-based efficiencies between the lactate method and our previous mitochondrial method, we evaluated the yield and found 52.9 ± 12.8% recovery of cardiomyocytes in our previous mitochondrial method (Figure S3I). To determine the types of noncardiomyocyte cells remaining after metabolic selection, we performed immunocytochemical screening and found that most of the cells were smooth muscle actin (SMA)-positive (Figure S3J). Interestingly, α-actinin- and SMA-double-positive cells were also found (data not shown), consistent with a previous report that immature cardiomyocytes express SMA (Clément et al., 2007).

We then applied the lactate method to mouse ESCs using lactate concentrations and timings optimized through similar preliminary experiments for mouse cells. EBs attached to the dishes were exposed to glucose-depleted and 1 mM lactate-supplemented conditions. After 7 days of selection, we recovered the surviving cells by collagenase digestion and transferred them into new fibronectin-coated plates (Movie S3). Immunofluorescence staining revealed that most of the surviving cells were positive for the cardiac markers α-actinin and GATA4 (99.4 ± 0.6% purity, n = 5) (Figure S3K).

Cardiomyocytes Showed High Lactate Uptake and Used Lactate for Metabolic-Energy Production

Why do only cardiomyocytes survive under the lactate-method condition? To address this question, we first compared the [^{14}C]-lactate uptake activity of neonatal rat and human ESC-derived cardiomyocytes, ESCs, MEFs, and noncontracting EBs, and found that both cardiomyocyte populations showed higher levels of activity than the other cells (Figures 4A and 4C). We then measured the changes in intracellular ATP levels in cardiomyocytes and other cells under lactate-method conditions and found that the levels in mouse ESCs, MEFs, and noncontracting EBs fell abruptly, whereas those in neonatal rat and purified human ESC-derived cardiomyocytes were sustained for significantly longer (Figures 4B and 4D). These results indicated that cardiomyocytes, but not noncardiomyocytes, can effectively uptake and use lactate to maintain ATP levels.

Lactate supplementation has the potential to cause acidification either intracellularly or in the medium, which could lead to cellular damage. We therefore investigated whether 4 mM lactate supplementation affects extra- and intracellular pH values. The extracellular pH values were stable at 7.5 following 1 hr of incubation in a 5% CO_2 incubator (Figure S4A). The intracellular pH values of cardiomyocytes, mouse ESCs, MEFs, and C2C12 myoblasts were not affected by supplementation with 4 mM lactate, but all were significantly decreased by the addition of 20 mM lactate (Figures S4B and S4C). Lactate can be transported by monocarboxylic acid transporters (MCTs), of which subtype 1 is abundantly expressed in muscle cells and localizes at both the plasma and mitochondrial inner membrane (Hashimoto et al., 2006). For investigation of the significance of MCT1 expression for lactate uptake in cardiomyocytes, the cells were treated with MCT1 inhibitor α-cyano-4-hydroxycinnamate (α-CHC) (Sonveaux et al., 2008) under glucose-free and lactate-rich conditions. The lactate-induced prolonged survival of cardiomyocytes under glucose-free conditions was largely abolished by the MCT1 inhibitor, despite the lack of α-CHC toxicity, suggesting that lactate uptake via MCT1 plays a major role in the long-term survival of cardiomyocytes under metabolic selection (Figure 4E). To investigate why cardiomyocytes can effectively take up lactate, we checked the expression levels of MCT1 in cardiomyocytes and ESCs but could not find a marked difference between the two (Table S1). We then performed electron microscopy on the hESCs and their derivative cardiomyocytes, as well as mitochondrial staining of hESC-derived cells. The cardiomyocytes showed substantially higher numbers of mitochondria than ESCs and other noncardiomyocytes (Figures S4D and S4E). Because MCTs are passive transporters, we suggest that a major mechanism underlying the enhanced lactate uptake in cardiomyocytes could be the concentration gradients generated by effective lactate consumption via the highly active TCA cycle.

We further investigated how lactate is metabolized in various types of cells. We performed lactate fluxome analysis in mouse ESCs, hESC-derived EBs, MEFs, and neonatal rat cardiomyocytes under glucose-depleted conditions for short (30 min) periods. As expected, high levels of [2,4,5-^{13}C]-citrate, [3,4-^{13}C]-succinate, and [2,3,4-^{13}C]-malate were detected in cardiomyocytes, whereas the ESCs, hESC-derived EBs, and MEFs showed only small amounts of these metabolites, suggesting that exogenous lactate is more efficiently metabolized via the TCA cycle in cardiomyocytes than in noncardiomyocytes, including ESCs (Figure 5 and Figure S5). To our surprise, [^{13}C]-labeled glycolytic intermediates including G6P were observed in both cardiomyocytes and ESCs. These were eventually consumed in the pentose phosphate pathway for production of inosine, guanosine, and adenosine monophosphates.

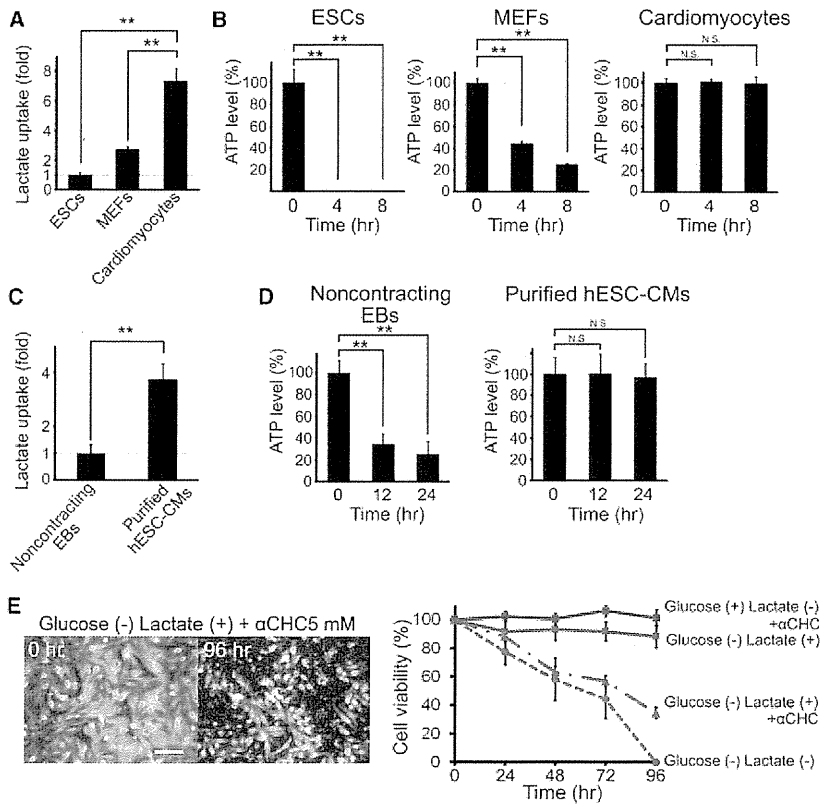

Figure 4. Lactate Uptake and Energetic Homeostasis in Various Types of Cells under Glucose-Depleted and Lactate-Supplemented Conditions

(A and C) [^{14}C]-labeled lactate uptake abilities in (A) mouse ESCs, MEFs, and rat neonatal cardiomyocytes (n = 3) and (C) in noncontracting hESC-derived EBs and purified hESC-CMs (n = 3). All data were obtained from independent experiments.

(B and D) Intracellular ATP levels in (B) the mouse ESCs, MEFs, and neonatal cardiomyocytes (n = 3), and (D) in noncontracting hESC-derived EBs and purified hESC-CMs (n = 3) under glucose-depleted and lactate-supplemented conditions. Relative ATP levels are indicated as percentages of the levels in untreated samples. All data were obtained from independent experiments.

(E) Cultured neonatal rat cardiomyocytes were exposed to glucose-free with lactate conditions supplemented with MCT1 inhibitor (α-CHC, 5 mM), and their viabilities were visualized using the LIVE/DEAD kit (left). The time course of the cardiomyocyte viabilities under different culture conditions is shown (right). Chain and solid red lines indicate glucose-depleted and lactate-supplemented medium supplemented with (n = 4) and without (n = 6) MCT1 inhibitor, respectively. The dashed red line indicates the glucose-depleted without lactate condition (n = 6). The blue solid line indicates high-glucose medium supplemented with MCT1 inhibitor (n = 4). All data were obtained from independent experiments.

Scale bar represents 100 μm (E). *$p < 0.05$; **$p < 0.01$. Data are shown as mean ± SD. See also Figure S4.

Long-period (24 hr) fluxome analysis in viable cardiomyocytes also detected [5-^{13}C]-labeled reduced (GSH) and [4,5,6,7,8, 10-^{13}C]-labeled oxidized glutathione (GSSG), indicating that glutamate, glycine, and/or cysteine were also synthesized from the lactate (Figure 5 and Table S2).

Purified hESC-Derived Cardiomyocytes Showed High Proliferative Capacity

We next investigated the proliferative capacity of mouse and human ESC-derived cardiomyocytes purified using metabolic selection. Some of the purified cardiomyocytes expressed Ki67 antigen (Figure 6A) and showed EdU-incorporation activities (Figure 6B). For directly assessing the rate of karyokinesis and cytokinesis after metabolic selection, the purified hESC-derived aggregates were completely dissociated and then seeded sparsely onto the MEF-layered dishes. Counting of immunocytochemically α-actinin-positive cells after 2, 4, 6, and 8 days revealed that the purified cardiomyocytes could proliferate up to 2.5-fold in 8 days, and the fraction of multinuclear cardiomyocytes increased over time compared with the second day (Figure 6C).

Purified Human PSC-derived Cardiomyocytes Showed Physiologically Relevant Action-Potential Configurations and Drug Responses

Action-potential recording using glass microelectrodes revealed that the purified hESC-derived cardiomyocytes had nodal- (14 of 76), atrial- (23 of 76), or ventricular-like (39 of 76) action potentials (Figure 6D and Figure S6A). We next evaluated their chronotropic response to the β-agonist isoproterenol and muscarinic agonist carbamylcholine using the multielectrode array (MEA) system; the former agent increased the beating frequency, whereas the latter decreased it, both in a dose-dependent manner (Figure 6E). We also found that beat frequency could be modulated by temperature (Figure S6B), and intracellular [Ca^{2+}] recording using Fluo-4 dye also revealed that the purified hESC-derived cardiomyocytes showed spontaneous and synchronized Ca^{2+} oscillations (Figure S6C).

Transplanted Purified Cardiomyocytes Did Not Form Tumors

Finally, for investigation of the potential tumorigenicity of the purified cardiomyocyte populations, 1,000 undifferentiated hESCs, 2.0×10^5 nonpurified hESC-derived cardiomyocytes, or the same number of purified cells were transplanted into the testes of immunocompromised nonobese diabetic severe combined immunodeficient (NOD-SCID) mice. Two months later, 9 of 10 (90%), 8 of 20 (40%), and 0 of 20 mice developed tumors, respectively (Figure 6F and Figure S6D). For further verification of the absence of residual undifferentiated cells, nonpurified and purified dispersed hESC-derived cells (2.0×10^5) were cultured on MEFs under PSC maintenance culture conditions (colony formation assay) for 4 days. Nonpurified hESC-derived cells formed Oct3/4- or Tra1-60-positive piled-up colonies, but

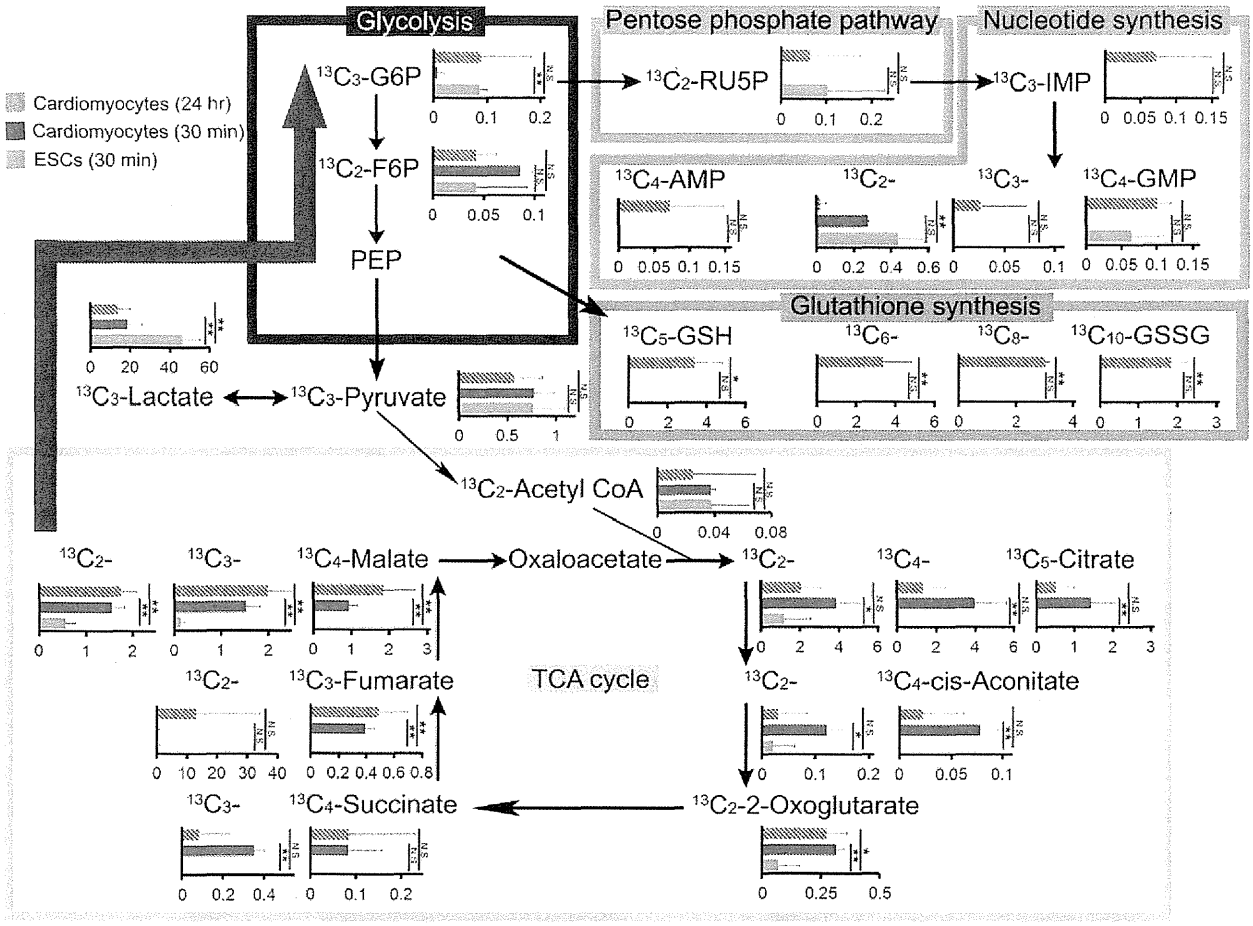

Figure 5. Mechanisms Underlying the Lactate-Mediated Survival of Cardiomyocytes

Fluxome analysis of the short-term (30 min) and long-term (24 hr) administration of [^{13}C]-labeled lactate under glucose-depleted conditions in neonatal cardiomyocytes and ESCs (ESCs, n = 4; cardiomyocytes, n = 3). The relationships between the kinds of bars, kinds of cell, and labeling conditions are shown in the upper left. All data were obtained from independent experiments. The bold red arrow on the right indicates a possible reflux pathway from malate to G6P. All units are nmol per 1.0 × 10^7 cells. *p < 0.05; **p < 0.01. Data are shown as mean ± SD. PEP, phosphoenolpyruvate. See also Figure S5 and Table S2.

the purified cardiomyocytes formed no colonies (Figure 6G and Figure S6E). To demonstrate the PSC-elimination capacity of the lactate method, we used a commercially available kit based on magnetic-beads-activated cell sorting with a Tra1-60 antibody. This experiment confirmed the apparent superiority of the lactate method in eliminating stem cells compared to the tested method (Figure S6F).

DISCUSSION

There are several approaches available for obtaining enriched cardiomyocyte populations from human PSCs. Ma et al. (2011) performed genetic-modification-based purification of cardiomyocytes (achieving >98% cardiomyocyte purity) from hiPSC derivatives, using the intrinsic *MYH6* gene to express a blasticidin S resistance gene. Dubois et al. (2011) used a surface protein, signal-regulatory protein alpha (SIRPA), as a cardiac-specific marker in hiPSC derivatives prepared through a highly cardiogenic differentiation procedure. They purified cardiomyocytes (up to 98% purity) via FACS from sources comprising 40%–50% cardiomyocytes. The method we report here is a simple medium-exchanging procedure that enabled cardiomyocyte purification of up to 99% from a cell source comprising only 10% cardiomyocytes, with an estimated recovery of cardiomyocytes of 74.4 ± 12.1%, based on direct cell count before and after purification. Previously we reported a mitochondrial method for purifying cardiomyocytes to >99% purity via FACS. Our direct comparison of these two methods revealed a higher cardiomyocyte-yield-based efficiency for the lactate method than for the mitochondrial method. The lactate method has quantitative and economic advantages relative to other existing cardiomyocyte-purification methods by virtue of its simplicity and ease of application.

One question that arose from our studies is why ESCs die within a few hours under the lactate method but cardiomyocytes survive for much longer, even though both cell types use lactate

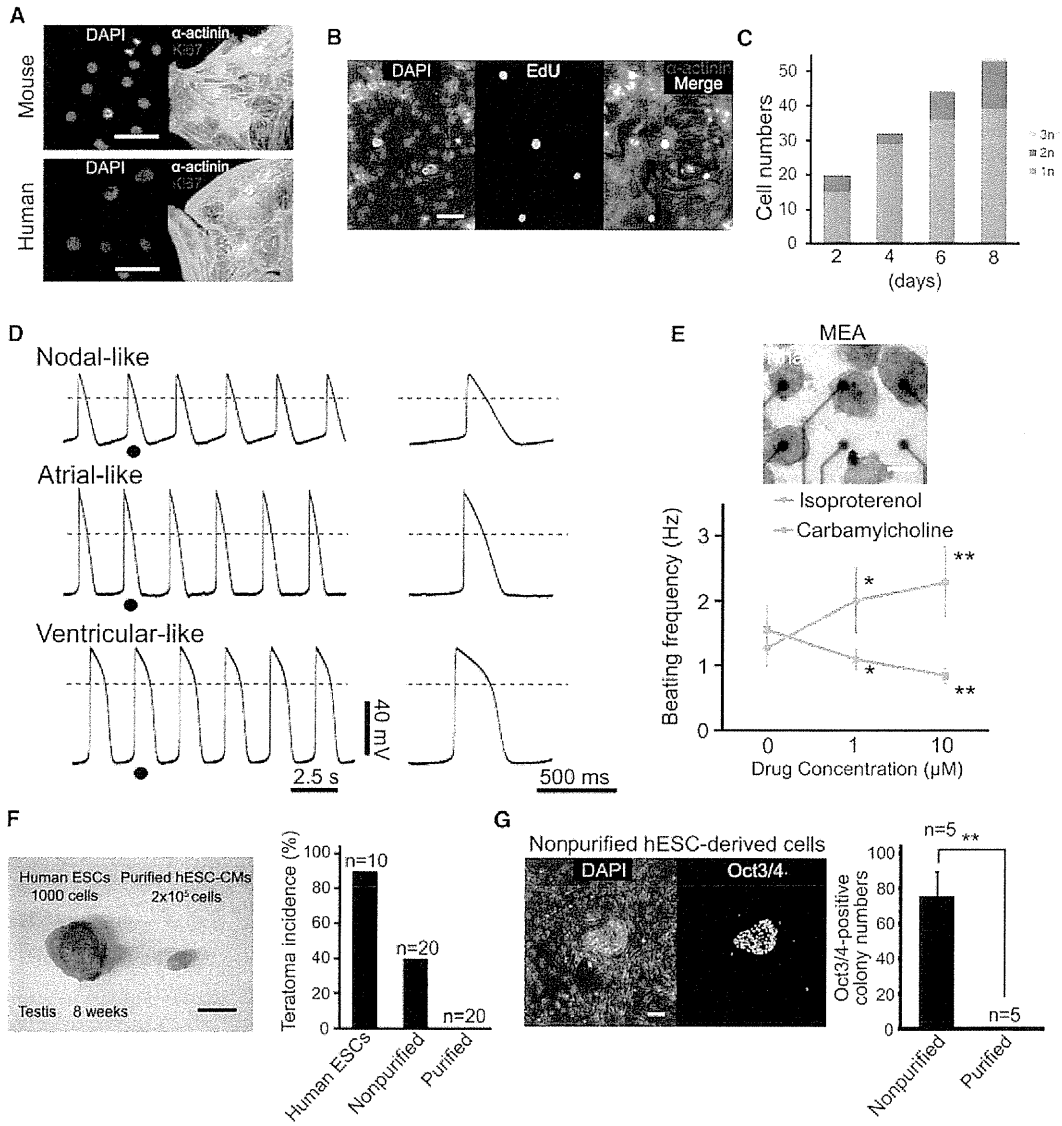

Figure 6. Characterization of ESC-Derived Cardiomyocytes after Metabolic Selection

(A) Immunofluorescent staining for α-actinin (green) and Ki67 (red) in the purified mouse (top) and human (bottom) ESC-CMs.

(B) EdU-positive cells (green) in purified hESC-CMs.

(C) Numbers of hESC-derived dispersed cardiomyocytes after metabolic selection. The numbers of cardiomyocytes with single, double, and more than triple nuclei are separately represented by the blue, red, and green bars, respectively.

(D) Action-potential recording of the purified hESC-CMs using microelectrodes. Shown are representative configurations of the nodal- (top), atrial- (middle), and ventricular-like (bottom) action potentials.

(E) Drug responses in purified hESC-derived aggregates using the MEA system (top). The line graph (bottom) represents the chronotropic response against β-agonist isoproterenol (green; n = 3) and muscarinic agonist carbamylcholine (orange; n = 3). All data were obtained from independent experiments.

(F) The teratoma-forming capacities of hESCs (1,000 cells), nonpurified hESC-derived cells (2.0×10^5 cells), and purified hESC-CMs (2.0×10^5 cells) were evaluated through their transplantation into the testes of NOD-SCID mice. The bar graph represents the summarized results (hESCs, n = 10; nonpurified, n = 20; purified, n = 20).

(G) Immunofluorescent staining for Oct3/4 in dispersed cells from nonpurified hESC-derived EBs. The bar graph shows numbers of hESC-like colonies obtained from hESC-derived cells (2.0×10^5; n = 5).

Scale bars represent 50 μm (A and B), 100 μm (E and G), and 1 cm (F). *p < 0.05; **p < 0.01. Data are shown as mean ± SD. See also Figure S6.

for biomass synthesis. Through our investigations, we eliminated the possibility that lactate supplementation caused toxic extracellular or intracellular acidification. We propose that these differing properties may be a result of (1) the retrospective glycolytic pathway consuming two ATP molecules during conversion of a lactate molecule to G6P, and (2) ESCs not being

able to effectively obtain ATP from glycolysis nor from OXPHOS under glucose-depleted conditions. Therefore, activation of the retrospective glycolytic pathway may accelerate a catastrophic balance of ATP supply and demand in ESCs, whereas cardiomyocytes can maintain cellular ATP homeostasis by producing more ATP via a highly active OXPHOS mechanism (Hattori et al., 2010).

A patient would theoretically require about 10^9 cardiomyocytes in therapeutic applications of purified cardiomyocytes. In this study, we obtained approximately 5×10^5 purified human cardiomyocytes per 177 cm^2 dish. Taking into account their postpurification proliferative capacities, rough estimates therefore suggest that 1×10^9 cardiomyocytes could be obtained from 800 dishes (14.13 m^2). This scale is close to the capacity of commercially available automatic large-scale culture systems and suggests that combining more sophisticated differentiation methods with our lactate method could facilitate realistic application of PSC-derived cardiomyocytes to human therapy.

EXPERIMENTAL PROCEDURES

Animals

All animals including pregnant ICR mice, neonatal Wistar rats, and NOD-SCID mice (8 weeks old, male) were purchased from CLEA Japan (Tokyo). All experimental procedures and protocols were approved by the Animal Care and Use Committee of Keio University and conformed to the National Institutes of Health Guide for the Care and Use of Laboratory Animals.

Cells

Mouse ESCs were obtained from the Laboratory of Pluripotent Cell Studies, RIKEN Center for Developmental Biology. The hESC line (KhES-2 and KhES-3) was obtained from the Department of Development and Differentiation, Institute for Frontier Medical Sciences, Kyoto University and used in conformity with the Guidelines for Derivation and Utilization of Human Embryonic Stem Cells of the Ministry of Education, Culture, Sports, Science, and Technology, Japan. The hiPSC line (253G4 and 201B7) was obtained from the Center for iPSC Research and Application, Kyoto University. The skeletal myoblast cell line (C2C12), hepatocyte cell line (HepG2), and renal cell line (HEK293) were obtained from the American Type Culture Collection.

Reagents

The mouse monoclonal antibodies for α-actinin (immunoglobulin G_1 [IgG_1]) and Ki67 (IgM) were purchased from Sigma-Aldrich (Sigma). The mouse monoclonal antibodies for SMA (IgG_{2a}), βIII-tubulin, Oct3/4, and Tra1-60 were purchased from Dako, Promega, BD Transduction Laboratories, and Millipore, respectively. The goat polyclonal antibodies for GATA-4 (C-20) and Nkx2.5 (N-19) were purchased from Santa Cruz Biotechnology (Santa Cruz). Alexa Fluor 488 and 546 anti-mouse IgG (IgG_1, IgG_{2a}, and IgM) antibody and anti-goat IgG antibody were purchased from Invitrogen. DAPI and E-cadherin-Fc were also purchased from Invitrogen. Tetramethylrhodamine methyl ester perchlorate (TMRM), mitotracker red, 2′,7′-bis-(2-carboxyethyl)-5-(and-6)-carboxyfluorescein (BCECF) and Fluo-4 dye were purchased from Invitrogen. Fibronectin, isoproterenol hydrochloride, carbamylcholine, and α-CHC were purchased from Sigma. The [^{13}C]-labeled glucose and lactate were purchased from Isotec. The [^{14}C]-labeled lactate was purchased from PerkinElmer.

Maintenance of Mouse and Human PSCs

We maintained mouse ESCs on gelatin- or E-cadherin-coated dishes in Glasgow minimum essential medium (MEM) (Sigma) supplemented with 10% fetal bovine serum (FBS; Equitech-Bio), 0.1 mM MEM nonessential amino acid solution (Sigma), 2 mM L glutamine (Sigma), 0.1 mM β-mercaptoethanol (Sigma), and 2,000 U/ml murine leukemia inhibitory factor (Chemicon) (Nagaoka et al., 2006). We maintained hESCs and hiPSCs on MEFs in Dulbecco's modified Eagle's medium/nutrient mixture F-12 Ham 1:1 (DMEM-F12; Sigma) supplemented with 20% knockout serum replacement (Invitrogen), 0.1 mM MEM nonessential amino acid solution (Sigma), 2 mM L glutamine (Sigma), 0.1 mM β-mercaptoethanol (Sigma), and 4 ng/ml basic fibroblast growth factor (Wako).

Differentiation of Human PSC-Derived Cardiomyocytes

We cultured the enzymatically detached undifferentiated colonies of hESCs and hiPSCs with αMEM (Wako Pure Chemical, Wako) that contained 50 μg/ml ascorbic acid, supplemented with 5% FBS (Biowest) and 0.1 mM β-mercaptoethanol in bacterial Petri dishes for formation of EBs. EBs containing rhythmically beating cells were observed 14 to 20 days later. Typically, 1%–10% of EBs contained beating cells. Media were changed once a week. EBs were used for purification experiments between days 20 and 30.

Purification of hESC- and hiPSC-Derived Cardiomyocytes

The selection medium was prepared before use. Glucose-free DMEM (no glucose, no pyruvate; Invitrogen) supplemented with 4 mM lactate medium was produced using 1 M lactate stock solution prepared from diluting 10 M lactate (Wako Pure Chemical) with sterile 1M Na-HEPES (Sigma). The human PSC-derived EBs at differentiation day 20 to 30 were extensively washed with and exposed to the selection medium. Media were changed every 2 or 3 days for eliminating dead cells via rapid flushing using 40 μm filters (Becton Dickinson). Cells were sampled daily from day 6 of purification for optimizing the timing of harvest for each batch. We split sampled cells into two experiments: one for test cultivation and another for FACS analysis. In the test cultivation, cells were transferred to fibronectin-coated dishes and cultured for several days with αMEM supplemented with 5% FBS. FACS analysis was performed using α-actinin antibodies. Our criterion for determining the harvest day was at least 95% purity indicated by FACS analysis. All harvested cells were then transferred to fibronectin-coated dishes and cultured for several more days under αMEM supplemented with 5% FBS, during which the media were changed several times for complete removal of debris consisting of dead cells and insoluble matrix. The purified cardiomyocytes were finally collected by rapid flushing. Movies were recorded using a fluorescence microscope (BZ-9000; Keyence).

Cardiomyocyte Purification Using Mitochondrial Dye for Gene Array

To prepare purified cardiomyocytes for the gene array, we used hearts from neonatal mice (P1). Purification of mouse neonatal cardiomyocytes using mitochondrial TMRM dye was performed by FACS (FACS Aria; Becton Dickinson), as described previously (Hattori et al., 2010).

Immunofluorescence

We fixed cells with 4% paraformaldehyde in PBS (pH 7.0) for 20 min. Subsequently, cells were permeabilized with 0.1% Triton X-100 (Sigma) at room temperature for 10 min and then incubated with the primary antibody at 4°C overnight. Cells were then washed with Tris-buffered saline (TBS) containing 0.1% Tween 20 four times prior to incubation with the secondary antibodies at room temperature for 1 hr. After nuclear staining with DAPI (Invitrogen), stained cells were detected by fluorescence microscopy (IX71; Olympus) or confocal-laser microscopy (LSM 5 DUO; Carl Zeiss).

Cell Viability under Glucose-Depleted Conditions with or without Lactate

Neonatal cardiomyocytes, ESCs, and noncardiomyocytes including MEFs, HepG2, HEK293, peripheral lymphatic cells, C2C12, skeletal myotubes, and fetal neurons were exposed to glucose-free DMEM (Invitrogen) supplemented with or without lactate (Wako). Cell viabilities were determined by the LIVE/DEAD Viability/Cytotoxicity Assay Kit (Invitrogen) based on the simultaneous determination of live and dead cells with the calcein AM and ethidium homodimer-1 probes. Fluorescence imaging of the cells (live cells were labeled green, whereas the nuclei of dead cells were labeled red) was performed with fluorescence microscopy (IX70 microscope; Olympus) equipped with a color charge-coupled device camera (CS220; Olympus). The green-labeled live area was measured using Image J. Relative cell viabilities were calculated in percentages, compared with those before treatment.

FACS Analysis Using Sarcomeric α-Actinin Antibody

Purified cardiomyocytes were completely dissociated by 0.25% trypsin-EDTA and then fixed with 4% paraformaldehyde for 10 min. Subsequently, cells were permeabilized with 0.1% Triton X-100 (Sigma) at room temperature for 10 min and then incubated with the sarcomeric α-actinin antibody (Sigma) for 3 hr. Cells were washed with TBS containing 0.1% Tween 20 prior to incubation with the Alexa Fluor 488 donkey anti-mouse IgG secondary antibody (Invitrogen) at room temperature for 2 hr. These cells were analyzed via FACS (EPICS XL; Beckman Coulter).

Quantitative Real-Time PCR

Total RNA was extracted with ISOGEN reagent (Nippon Gene), and real-time PCR was performed as described previously (Yuasa et al., 2005). For quantitative analysis, complementary DNA (cDNA) was used as the template in a TaqMan real-time PCR assay using the ABI Prism 7700 sequence detection system (Applied Biosystems, Foster City, CA, USA) according to the manufacturer's instructions. Data were normalized to *GAPDH*. Human heart, skeletal muscle, and brain total RNA was purchased from Takara Bio. The primers and TaqMan probe for human *NANOG*, *POU5F1*, *ACTC1*, *NKX2.5*, *MYH6*, *MYOD*, *AFP*, *MAP2*, and *GAPDH* were Hs02387400_g1, Hs01895061_u1, Hs00606316_m1, Hs00231763_m1, Hs00411908_m1, Hs02330075_g1, Hs01040607_m1, Hs00258900_m1, and Hs02758991_g1, respectively.

Glucose Fluxome Analysis by Capillary Electrophoresis and Mass Spectrometry

In neonatal cardiomyocytes, ESCs, and noncardiomyocytes including HepG2 and C2C12, the media were switched to modified DMEM supplemented with 10% FBS and 10 mM [^{13}C]-labeled glucose (Isotec) instead of 10 mM glucose. In 30 min, these cells were washed in 10% mannitol (Wako) and then plunged into methanol that contained internal standards (300 μM each of methionine sulfone for cations and MES for anions). Cells and the medium were collected for capillary electrophoresis and mass spectrometry experiments using an Agilent capillary electrophoresis system equipped with an air pressure pump, an Agilent 1100 series mass selective detector mass spectrometer, an Agilent 1100 series isocratic high-performance liquid-chromatography pump, a G1603A Agilent capillary electrophoresis and mass spectrometry adaptor kit, and a G1607A Agilent capillary electrophoresis and mass spectrometry sprayer kit (Agilent Technologies) as described previously (Endo et al., 2009; Shintani et al., 2009). Values were corrected against cell numbers.

Lactate Fluxome Analysis by Capillary Electrophoresis and Mass Spectrometry

In mouse ESCs, hESC-derived EBs, MEFs, and neonatal rat cardiomyocytes, the medium was switched to modified glucose-free DMEM (Invitrogen) supplemented with 4 mM [^{13}C]-labeled lactate (Isotec). After 30 min and/or 24 hr, these cells were collected for analysis as described above. Values were corrected against cell numbers.

Action-Potential Recordings Using Microelectrodes

The microscope was equipped with a recording chamber and a noise-free heating plate (Micro Warm Plate; Kitazato Supply). Standard glass microelectrodes that had a DC resistance of 25–35 mega Ω when filled with pipette solution (2 M KCl) were positioned using a motor-driven micromanipulator (EMM-3SV; Narishige) under optical control. Spontaneously contracting hESC-derived aggregates after metabolic selection were seeded and cultured in fibronectin-coated dishes, and the action potentials were recorded. The recording pipette was connected to a patch-clamp amplifier (Axopatch 200B; Axon Instruments), and the signal was passed through a low-pass filter with a cutoff frequency of 2 kHz and digitized using an A/D converter with a sampling frequency of 10 kHz (Digidata 1440A; Axon Instruments). Signals were monitored, recorded as electronic files, and then analyzed offline with pCLAMP 10 software (Axon Instruments).

Field-Potential Recordings Using the MEA System

To characterize the functional properties of our purified human PSC-derived cardiomyocytes, we performed extracellular recording of field potentials using the MEA system (Multi Channel Systems, Reutlingen, Germany) as described previously (Tanaka et al., 2009; Zwi et al., 2009). To assess the effects of different drugs on the electrophysiological properties, drug-diluted medium was applied to the MEA culture plate. The applied drugs included isoproterenol hydrochloride and carbamylcholine. The temperature was maintained at 37°C during these recordings. For further evaluation of the effects of temperature on the electrophysiological properties, temperatures were also varied from 30°C to 42°C.

Teratoma Formation

To verify the elimination of immature cells with the potential to form teratomas by purification, we transplanted 2.0 × 10^5 purified hESC-derived cardiomyocytes, 2.0 × 10^5 nonpurified hESC-derived cells, and 1,000 undifferentiated hESCs into the testes of immunocompromised NOD-SCID mice. Two months after transplantation, animals were euthanized, and teratoma incidence was evaluated.

Colony-Formation Assay

Nonpurified and purified hESC-derived cells (2.0 × 10^5) were completely dissociated and cultured on the MEFs with PSC maintenance culture condition with 10 μM of ROCK inhibitor for 4 days. Then, immunofluorescence staining for Oct3/4 and Tra1-60 was performed, and colony numbers were counted.

ATP Measurement

Cells were plated onto gelatin-coated 96-well white, clear-bottom culture plates (Costar). After 2 days, cells were treated with the glucose-free plus lactate medium for a given length of time. ATP levels were measured using an ATP assay kit (Toyo Ink). In brief, 100 μl of the lysis and assay solution provided by the manufacturer was added to the wells. After shaking for 1 min and incubating for 20 min at 23°C, we measured luminescence of an aliquot of the solution in a luminometer (Synergy 4; BioTek).

[^{14}C]-Labeled Lactate Uptake

After washing the plates in glucose-free medium, cells were exposed to the glucose-free plus 1 μM [^{14}C]-labeled lactate condition. After 30 min, the cells were washed three times in fresh medium and collected for analysis. [^{14}C] signal was detected by liquid scintillation analysis (Packard). Values were corrected against cell number.

EdU Incorporation Assay

In one case, purified hESC-derived cardiomyocytes were dispersed and seeded in the MEF precultured dishes and cultured with αMEM containing 5% FBS for 12 hr for attachment. They were then treated with 10 μM EdU for 48 hr and processed according to the manufacturer's instructions (Invitrogen, Click-iT EdU Alexa Fluor 488 kit). The cells then underwent additional immunofluorescent staining for α-actinin and were observed by fluorescence microscopy. In another experimental setting, the intact floating hESC-derived EBs were treated with 10 μM EdU for 48 hr, dispersed, and then fixed with 4% paraformaldehyde followed by FACS analysis for determining the percentage of EdU-incorporated cells.

Statistical Analysis

All statistical analyses were performed using the Statistical Package for the Social Sciences for Windows version 17 software (SPSS, Chicago). Values are presented as mean ± SD. The statistical significance was evaluated using Student's t tests. A p value of less than 0.05 was considered statistically significant.

SUPPLEMENTAL INFORMATION

Supplemental Information includes six figures, two tables, three movies, and Supplemental Experimental Procedures and can be found with this article online at http://dx.doi.org/10.1016/j.stem.2012.09.013.

ACKNOWLEDGMENTS

We thank K. Sekine in the Department of Anatomy, Keio University School of Medicine for technical assistance with primary culturing of neurons. This study was mainly supported by the Strategic Funds for the Promotion of Science and Technology of the Japanese Ministry of Education Sports, Science, and

Technology (MEXT) and the Highway Program for the Realization of Regenerative Medicine and partially supported by a Japan Heart Foundation research grant, the Japan Science and Technology Agency (JST), Exploratory Research for Advanced Technology (ERATO), Suematsu Gas Biology Project, and a research grant from Asubio Pharma. F.H., T.T., and M.Y. are the employees and H.Y. is an indirect employee of Asubio Pharma Co., Ltd.

Received: July 31, 2011
Revised: May 10, 2012
Accepted: September 13, 2012
Published online: November 15, 2012

REFERENCES

Ashburner, M., Ball, C.A., Blake, J.A., Botstein, D., Butler, H., Cherry, J.M., Davis, A.P., Dolinski, K., Dwight, S.S., Eppig, J.T., et al.; The Gene Ontology Consortium. (2000). Gene ontology: tool for the unification of biology. Nat. Genet. *25*, 25–29.

Burd, L.I., Jones, M.D., Jr., Simmons, M.A., Makowski, E.L., Meschia, G., and Battaglia, F.C. (1975). Placental production and foetal utilisation of lactate and pyruvate. Nature *254*, 710–711.

Burridge, P.W., Keller, G., Gold, J.D., and Wu, J.C. (2012). Production of de novo cardiomyocytes: human pluripotent stem cell differentiation and direct reprogramming. Cell Stem Cell *10*, 16–28.

Clément, S., Stouffs, M., Bettiol, E., Kampf, S., Krause, K.H., Chaponnier, C., and Jaconi, M. (2007). Expression and function of alpha-smooth muscle actin during embryonic-stem-cell-derived cardiomyocyte differentiation. J. Cell Sci. *120*, 229–238.

Dubois, N.C., Craft, A.M., Sharma, P., Elliott, D.A., Stanley, E.G., Elefanty, A.G., Gramolini, A., and Keller, G. (2011). SIRPA is a specific cell-surface marker for isolating cardiomyocytes derived from human pluripotent stem cells. Nat. Biotechnol. *29*, 1011–1018.

Endo, J., Sano, M., Katayama, T., Hishiki, T., Shinmura, K., Morizane, S., Matsuhashi, T., Katsumata, Y., Zhang, Y., Ito, H., et al. (2009). Metabolic remodeling induced by mitochondrial aldehyde stress stimulates tolerance to oxidative stress in the heart. Circ. Res. *105*, 1118–1127.

Fijnvandraat, A.C., van Ginneken, A.C., Schumacher, C.A., Boheler, K.R., Lekanne Deprez, R.H., Christoffels, V.M., and Moorman, A.F. (2003). Cardiomyocytes purified from differentiated embryonic stem cells exhibit characteristics of early chamber myocardium. J. Mol. Cell. Cardiol. *35*, 1461–1472.

Fisher, D.J., Heymann, M.A., and Rudolph, A.M. (1981). Myocardial consumption of oxygen and carbohydrates in newborn sheep. Pediatr. Res. *15*, 843–846.

Gassanov, N., Er, F., Zagidullin, N., and Hoppe, U.C. (2004). Endothelin induces differentiation of ANP-EGFP expressing embryonic stem cells towards a pacemaker phenotype. FASEB J. *18*, 1710–1712.

Hashimoto, T., Hussien, R., and Brooks, G.A. (2006). Colocalization of MCT1, CD147, and LDH in mitochondrial inner membrane of L6 muscle cells: evidence of a mitochondrial lactate oxidation complex. Am. J. Physiol. Endocrinol. Metab. *290*, E1237–E1244.

Hattori, F., and Fukuda, K. (2012). Strategies for replacing myocytes with induced pluripotent stem in clinical protocols. Transplant Rev. (Orlando) *26*, 223–232.

Hattori, F., Chen, H., Yamashita, H., Tohyama, S., Satoh, Y.S., Yuasa, S., Li, W., Yamakawa, H., Tanaka, T., Onitsuka, T., et al. (2010). Nongenetic method for purifying stem cell-derived cardiomyocytes. Nat. Methods *7*, 61–66.

Hidaka, K., Lee, J.K., Kim, H.S., Ihm, C.H., Iio, A., Ogawa, M., Nishikawa, S., Kodama, I., and Morisaki, T. (2003). Chamber-specific differentiation of Nkx2.5-positive cardiac precursor cells from murine embryonic stem cells. FASEB J. *17*, 740–742.

Kinoshita, A., Tsukada, K., Soga, T., Hishiki, T., Ueno, Y., Nakayama, Y., Tomita, M., and Suematsu, M. (2007). Roles of hemoglobin Allostery in hypoxia-induced metabolic alterations in erythrocytes: simulation and its verification by metabolome analysis. J. Biol. Chem. *282*, 10731–10741.

Klug, M.G., Soonpaa, M.H., Koh, G.Y., and Field, L.J. (1996). Genetically selected cardiomyocytes from differentiating embronic stem cells form stable intracardiac grafts. J. Clin. Invest. *98*, 216–224.

Laflamme, M.A., Chen, K.Y., Naumova, A.V., Muskheli, V., Fugate, J.A., Dupras, S.K., Reinecke, H., Xu, C., Hassanipour, M., Police, S., et al. (2007). Cardiomyocytes derived from human embryonic stem cells in pro-survival factors enhance function of infarcted rat hearts. Nat. Biotechnol. *25*, 1015–1024.

Ma, J., Guo, L., Fiene, S.J., Anson, B.D., Thomson, J.A., Kamp, T.J., Kolaja, K.L., Swanson, B.J., and January, C.T. (2011). High purity human-induced pluripotent stem cell-derived cardiomyocytes: electrophysiological properties of action potentials and ionic currents. Am. J. Physiol. Heart Circ. Physiol. *301*, H2006–H2017.

Nagaoka, M., Koshimizu, U., Yuasa, S., Hattori, F., Chen, H., Tanaka, T., Okabe, M., Fukuda, K., and Akaike, T. (2006). E-cadherin-coated plates maintain pluripotent ES cells without colony formation. PLoS ONE *1*, e15.

Neely, J.R., and Morgan, H.E. (1974). Relationship between carbohydrate and lipid metabolism and the energy balance of heart muscle. Annu. Rev. Physiol. *36*, 413–459.

Passier, R., van Laake, L.W., and Mummery, C.L. (2008). Stem-cell-based therapy and lessons from the heart. Nature *453*, 322–329.

Shintani, T., Iwabuchi, T., Soga, T., Kato, Y., Yamamoto, T., Takano, N., Hishiki, T., Ueno, Y., Ikeda, S., Sakuragawa, T., et al. (2009). Cystathionine beta-synthase as a carbon monoxide-sensitive regulator of bile excretion. Hepatology *49*, 141–150.

Sonveaux, P., Végran, F., Schroeder, T., Wergin, M.C., Verrax, J., Rabbani, Z.N., De Saedeleer, C.J., Kennedy, K.M., Diepart, C., Jordan, B.F., et al. (2008). Targeting lactate-fueled respiration selectively kills hypoxic tumor cells in mice. J. Clin. Invest. *118*, 3930–3942.

Takahashi, K., Tanabe, K., Ohnuki, M., Narita, M., Ichisaka, T., Tomoda, K., and Yamanaka, S. (2007). Induction of pluripotent stem cells from adult human fibroblasts by defined factors. Cell *131*, 861–872.

Tanaka, T., Tohyama, S., Murata, M., Nomura, F., Kaneko, T., Chen, H., Hattori, F., Egashira, T., Seki, T., Ohno, Y., et al. (2009). In vitro pharmacologic testing using human induced pluripotent stem cell-derived cardiomyocytes. Biochem. Biophys. Res. Commun. *385*, 497–502.

Thomson, J.A., Itskovitz-Eldor, J., Shapiro, S.S., Waknitz, M.A., Swiergiel, J.J., Marshall, V.S., and Jones, J.M. (1998). Embryonic stem cell lines derived from human blastocysts. Science *282*, 1145–1147.

Uosaki, H., Fukushima, H., Takeuchi, A., Matsuoka, S., Nakatsuji, N., Yamanaka, S., and Yamashita, J.K. (2011). Efficient and scalable purification of cardiomyocytes from human embryonic and induced pluripotent stem cells by VCAM1 surface expression. PLoS ONE *6*, e23657.

Werner, J.C., and Sicard, R.E. (1987). Lactate metabolism of isolated, perfused fetal, and newborn pig hearts. Pediatr. Res. *22*, 552–556.

Xu, C., He, J.Q., Kamp, T.J., Police, S., Hao, X., O'Sullivan, C., Carpenter, M.K., Lebkowski, J., and Gold, J.D. (2006). Human embryonic stem cell-derived cardiomyocytes can be maintained in defined medium without serum. Stem Cells Dev. *15*, 931–941.

Yuasa, S., Itabashi, Y., Koshimizu, U., Tanaka, T., Sugimura, K., Kinoshita, M., Hattori, F., Fukami, S., Shimazaki, T., Ogawa, S., et al. (2005). Transient inhibition of BMP signaling by Noggin induces cardiomyocyte differentiation of mouse embryonic stem cells. Nat. Biotechnol. *23*, 607–611.

Zwi, L., Caspi, O., Arbel, G., Huber, I., Gepstein, A., Park, I.H., and Gepstein, L. (2009). Cardiomyocyte differentiation of human induced pluripotent stem cells. Circulation *120*, 1513–1523.